Journal of Asian Earth Sciences 106 (2015) 19–33

Contents lists available at ScienceDirect

Journal of Asian Earth Sciences

journal homepage: www.elsevier.com/locate/jseaes

Petrogenesis of OIB-like basaltic volcanic rocks in a continental collision zone: Late Cenozoic magmatism of Eastern Iran

M. Kheirkhah [a], I. Neill [b,*], M.B. Allen [b]

[a] Research Institute for Earth Sciences, Geological Survey of Iran, Azadi Square, Meraj Avenue, Tehran, Iran
[b] Department of Earth Sciences, Durham University, South Road, Durham DH1 3LE, UK

ARTICLE INFO

Article history:
Received 21 October 2014
Received in revised form 13 February 2015
Accepted 24 February 2015
Available online 16 March 2015

Keywords:
Adakite
Collision
Geochemistry
Intraplate basalt
Iran

ABSTRACT

Hundreds of compositionally diverse volcanoes have erupted on the Turkish–Iranian Plateau in the last 15 Myr, attributed to one or more of the processes of Middle Miocene Tethyan slab break-off, localised lithospheric delamination and small-scale convection. Magmatism post-dates the initial Late Eocene or Early Oligocene Arabia–Eurasia collision by >10 Myr. By contrast, in the east of the plateau in Eastern Iran there has been intermittent magmatism from the Late Oligocene to the Quaternary. Magma types include alkali basalt flows and scoria cones and adakite-like intermediate–felsic lavas and domes. New elemental and Nd–Sr–Pb–Hf isotope data from Quaternary mafic alkaline flows near Quchan in the Meshkan area in the NE of the country are combined with existing data from Miocene–Quaternary volcanic centres in the Binalud Range and the Nayband/Neh Fault zones. These mafic, incompatible element-enriched rocks, with positive Nb–Ta anomalies, are OIB-like and are argued to have formed by low-degree melting of a heterogeneous mantle source which contained DMM- and EMII-like components. At least some of the melting took place in the garnet stability field. Significant crustal contamination during magma ascent is recognised in the Nayband/Neh samples. Penecontemporaneous adakite-like rocks are argued to be high-pressure fractionates of basaltic melts which may have a separate source to the OIB-like basalts. Late Cenozoic mantle melting was aided by (1) localised extension and (2) enhanced small-scale asthenospheric convection related to Makran subduction, low mantle viscosity owing to the prior Tethyan subduction history of the region, and possibly edge-driven convection on the margin of the thickened Zagros lithosphere.

1. Introduction

Continental collision results in extensive magmatic activity not necessarily related to widespread extension or orogenic collapse. This activity has been termed 'post-orogenic' (Turner et al., 1992) or 'collision zone' (Allen et al., 2013a) magmatism. The production of mafic collision zone magmas is commonly linked with lithospheric thinning (e.g., Pearce et al., 1990; Turner et al., 1992), or to mantle upwelling following break-off of the down-going oceanic slab (Davies and von Blanckenburg, 1995). Magmatism has also been associated with dewatering of hydrous phases in the lithospheric mantle (e.g., Allen et al., 2013a; Kheirkhah et al., 2013), melting of deeply-subducted continental crust (Zhao et al., 2013) and small-scale sub-lithospheric convection (Kaislaniemi et al., 2014). Mantle-derived collision zone magmas are documented for many Phanerozoic orogenic belts including Tibet (Williams et al., 2004), Taiwan (Wang et al., 2004), the Sulu Orogen (Zhang et al., 2010), the Hercynides (Seltmann et al., 2011) and the Caledonides (Atherton and Ghani, 2002).

The Turkish–Iranian Plateau formed in the Late Cenozoic across what is now Eastern Anatolia (Turkey), Southern Georgia, Armenia, Azerbaijan and Iran as a response to Arabia–Eurasia collision. The region is a prime site for the study of collision magmatism, being a young part of the Alpine–Himalayan belt with abundant and reasonably well-studied volcanic and intrusive rocks (Fig. 1a). There is also an ever-improving geophysical dataset which can be used to link magmatism to geodynamic processes (e.g., Angus et al., 2006; Zor, 2008; Priestley et al., 2012; Motaghi et al., in press). Most collision magmatism in the plateau has an incompatible element-enriched calc-alkaline or shoshonitic signature with trace element evidence for the presence of subduction-modified lithospheric mantle sources (Pearce et al., 1990; Kheirkhah et al., 2009; Dilek et al., 2010; Neill et al., 2013a). Magmatic activity has been variously linked to the processes above (Pearce et al.,

* Corresponding author at: School of Geographical and Earth Sciences, University of Glasgow, UK. Tel.: +44 1413 305477.
E-mail address: iain.neill@glasgow.ac.uk (I. Neill).

http://dx.doi.org/10.1016/j.jseaes.2015.02.027
1367-9120/

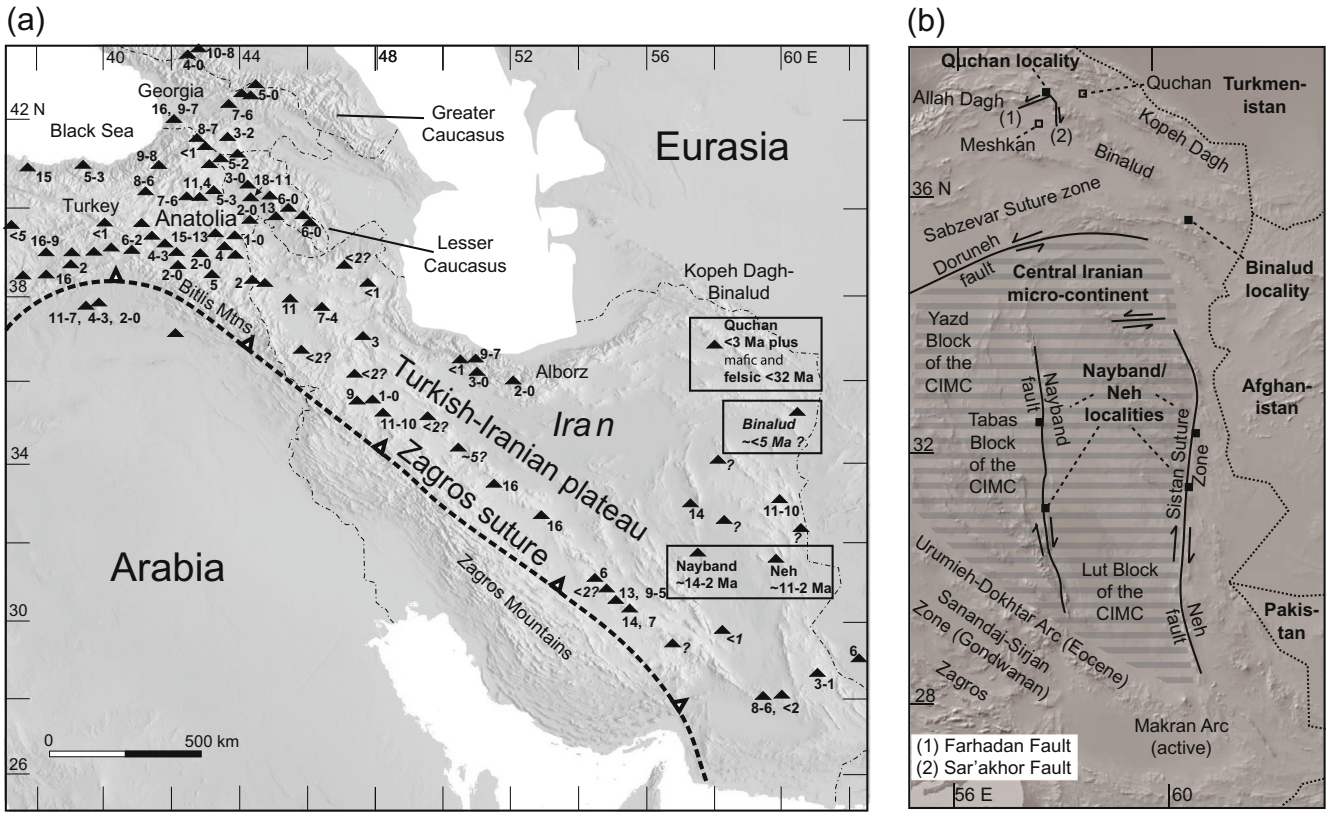

Fig. 1. (a) Map of the Turkish–Iranian Plateau after Neill et al. (2013a) and Kaislaniemi et al. (2014) showing ages of Middle Miocene to recent magmatism across the plateau, plus ages of Oligocene to recent magmatism discussed in the text. (b) Zoomed-in map showing the study area, including large strike-slip faults, major terranes and the location of mountains and towns mentioned in the text. Basemap for (b) is from GeoMapApp (http://www.geomapapp.org; Ryan et al., 2009; Haxby et al., 2010).

1990; Keskin, 2003; Pang et al., 2013; Allen et al., 2013a; Neill et al., 2013a; Kheirkhah et al., 2013; Kaislaniemi et al., 2014). However, there are several Late Cenozoic mafic volcanic centres on the plateau in Eastern Iran (Fig. 1b) which have an unusual geochemical signature, with high LREE (light rare earth element) and HFSE (high field strength element) and low HREE (heavy REE) abundances similar to ocean island basalts (OIBs) (Walker et al., 2009; Saadat et al., 2010; Pang et al., 2012; Saadat and Stern, 2012).

Such magma types are commonly regarded as 'anorogenic', and unrelated to the broad collision zones that host them, relating instead to asthenospheric flow (including putative mantle plumes), extension or the far-field effect subduction in locations such as Western Europe, Turkey, the Baikal Rift, Mongolia and NE China (e.g., Barry and Kent, 1998; Aldanmaz et al., 2006; Lebedev et al., 2006; Wilson and Downes, 2006; Lustrino and Wilson, 2007; Zhao et al., 2009; Beccaluva et al., 2011). In this study we re-assess the petrogenesis of the Late Cenozoic mafic rocks of Eastern Iran and their relationship to penecontemporaneous felsic, adakite-like volcanic and hypabyssal rocks (Shabanian et al., 2012) and the wider geodynamics of the Iranian Plateau.

2. Geological setting

2.1. Regional geology

Before the Paleogene Arabia–Eurasia collision, the Eurasian margin had already recorded the accretion of various terranes derived from the northern margin of Gondwana, notably the micro-continental blocks known collectively as the Cimmeride continent (Şengör, 1984) or more locally the Central Iranian Micro-Continent (e.g., Shojaat et al., 2003) (Fig. 1b). The oldest igneous and metamorphic rocks were created during the Late Proterozoic Pan-African orogeny at the margin of Gondwanaland. These basement lithologies are overlain by a Palaeozoic platform sequence, which records regional subsidence of the juvenile crust (Holt et al., 2010). Early Mesozoic (Palaeo-Tethyan) accretion was followed by rifting in the Cretaceous, which led to the creation of several narrow oceanic tracts which closed in the Late Cretaceous – Early Tertiary, producing ophiolite belts such as Khoy, Anar, Baft and Sabzevar (e.g., Shojaat et al., 2003). Neo-Tethyan subduction was directed northwards under the Gondwanaland-related Sanandaj–Sirjan Zone (Fig. 1b), beginning in the Jurassic and terminating with the Arabia–Eurasia collision in the Early Tertiary, but interrupted by Late Cretaceous ophiolite obduction onto the Arabian margin (Shahabpour, 2005; Chiu et al., 2013). The northward movement of Arabia and ultimate closure of the southern branch of Neo-Tethys resulted in initial collision with the Eurasian margin probably in the Latest Eocene – Early Oligocene (Allen and Armstrong, 2008; see McQuarrie and van Hinsbergen, 2013 for discussion). Deposition of marine carbonates across a large part of Iran and southern Turkey during the Early Miocene is taken to indicate regional subsidence during steepening of the subducted oceanic slab, before slab break-off (Bottrill et al., 2012). The Turkish–Iranian Plateau was then built from the Middle–Late Miocene onwards, following a combination of break-off beneath southern Turkey and NW Iran (Zor, 2008) and continued under-thrusting of the Arabian margin beneath the Zagros Suture further south in Iran (Paul et al., 2010). The present plateau covers an area of ~1,500,000 km^2 and undergoes little internal shortening, with continued Arabia–Eurasia convergence being concentrated in the lower elevation regions of mountain belts to its north and south (Vernant et al., 2004; Allen et al.,

2013b). Active deformation within the plateau is focussed on strike-slip faults. In Eastern Iran, our area of interest, these faults act as the margin of the collision zone and separate it from the relatively stable region of Afghanistan further east (Walker and Jackson, 2004) (Fig. 1b).

Eastern Iran covers a large part of the south and east of the plateau including the Lut Block (part of the Central Iranian Micro-continent), the Makran Arc in the south, the Sistan Suture Zone in the east and the Kopeh Dagh-Binalud mountain ranges in the north (Fig. 1). Basement lithologies are correspondingly varied, ranging from Proterozoic metamorphic and igneous rocks to Mesozoic–Paleogene sediments and arc-related volcanic-intrusive rocks and dismembered fragments of ophiolites. Aside from the still-active Makran Arc (Saadat and Stern, 2011; Pang et al., 2014), the last magmatism directly related to Neo-Tethyan subduction processes prior to initial Arabia–Eurasia collision took place during the Eocene (Emami et al., 1993; Allen and Armstrong, 2008), although Chiu et al. (2013) argue for continued subduction-related activity until the Late Miocene in the southern part of the Urumieh–Dokhtar Arc (Fig. 1). From Oligocene to recent times, there has been no arc-related magmatism in Eastern Iran, our area of interest. Instead there has been sporadic adakitic and OIB-like activity, as introduced in Section 2.2. Fig. 2 gives a schematic overview of the magmatic record of Eastern Iran since the termination of local subduction-related activity and the onset of the Arabia–Eurasia collision.

2.2. Late Cenozoic magmatism in Eastern Iran

2.2.1. Quchan

Late Cenozoic felsic and mafic volcanic and intrusive rocks are widespread to the southwest of Quchan (Fig. 1b) in the Meshkan Triangle, a tectonic wedge separating the Kopeh Dagh and Binalud mountain ranges (Shabanian et al., 2012). The 'triangle' is bounded on its north and east sides by the Farhadan and Sar'akhor faults which have generated a localised region of extension marked by magmatic activity (Fig. 1b). The felsic rocks in this area consist of trachyandesites, dacites and rhyolite domes including the 2500 m-high Sar'akhor volcano (Spies et al., 1983; Bauman et al., 1983; Ghasemi et al., 2010; Shabanian et al., 2012). K–Ar dating indicates that felsic magmatism took place in several stages, with 15 ages ranging from 31.7 ± 1.6 Ma to 2.29 ± 0.08 Ma (Fig. 2; Ghasemi et al., 2010). Geochemically the felsic rocks show affinities with adakites (see Section 5.4). The mafic rocks reported from within the Meshkan Triangle are arc-like (Shabanian et al., 2012) and K–Ar age dating of three samples gave Oligocene–Miocene ages of 26.2 ± 1.3 Ma, 19.5 ± 0.5 Ma and 18.5 ± 0.9 Ma, penecontemporaneous with the felsic magmatism (Fig. 2; Ghasemi et al., 2010).

In addition, an area of around 24 km^2 is partly covered by mafic alkaline flows, south–west of the towns of Faruj and Quchan (Fig. 1b) and just to the north of the left-lateral Farhadan fault. These do not appear to have been discussed in recent literature and were sampled specifically for this study. Individual flows have thicknesses of >10 m in some cases. The flows are reddish brown/black in colour and vary from smooth and blocky to vesicular and more fragmented in appearance. The flows overlie the Early Cretaceous Tirgan limestone as well as unconsolidated Pliocene conglomerates, indicating a likely Pliocene–Quaternary age (Geological Survey of Iran, 1984). These Quchan rocks therefore significantly post-date Eocene subduction-related magmatism and are very much younger than the majority of collision magmatism across much of the rest of the Turkish–Iranian Plateau, which flared up from the Middle Miocene onwards (<15–11 Ma) (e.g., Chiu et al., 2013; Pang et al., 2013). Samples from these flows consist of olivine- ± clinopyroxene-phyric basalts with 0.5–2 mm phenocrysts set in a fine groundmass containing olivine, clinopyroxene and rare amphibole micro-phenocrysts along with Fe–Ti oxides and large volumes of acicular plagioclase microlites. Clots of clinopyroxene and olivine form an obvious glomeroporphyritic texture in many samples indicating several phases of magma evolution. Small vesicles of 2–3 mm diameter are sometimes filled with quartz and calcite and many olivines are partially replaced by iddingsite, but otherwise the rocks appear reasonably fresh.

2.2.2. Binalud Range

An alkali basalt volcanic cone a few hundred metres across is recorded from the far SE of the Binalud Range (Fig. 1b) (Saadat and Stern, 2012; Su et al., 2014). This basalt contains a cargo including lower crustal gabbros and plagioclase megacrysts as well as fresh spinel lherzolite xenoliths and fragmented olivine and pyroxene xenocrysts apparently from disaggregated xenoliths (Saadat and Stern, 2012). Mantle xenoliths have not been found and described in detail from anywhere else in the Late Cenozoic record of Iran or Eastern Anatolia. The exact age of the basalt host is uncertain although the cone overlies Neogene sediments (Saadat and Stern, 2012). The presence of hot springs and travertines in the region may indicate a very young age for the basalt (Fig. 2). The basalt itself is described by Saadat and Stern (2012) as olivine-phyric, with plagioclase and rarely clinopyroxene phenocrysts.

2.2.3. Nayband and Neh Fault systems

Several scoria cones and mafic flows covering a few tens of km^2 each were erupted along the strike of the Nayband and Neh transform faults on the margins of the Lut Desert in south-eastern Iran (Walker et al., 2009; Saadat et al., 2010; Pang et al., 2012). Whole-rock Ar–Ar dating indicates that eruption of mafic rocks occurred over a long time period between ~14 and 1.6 Ma (Walker et al., 2009; Pang et al., 2012), although a single felsic sample was dated to 27.5 ± 0.5 Ma (Walker et al., 2009) (Fig. 2). The mafic rocks described from both the Nayband and Neh faults by Saadat et al. (2010) and Pang et al. (2012) have a few 10's of vol.% olivine, clinopyroxene and plagioclase phenocrysts in most samples.

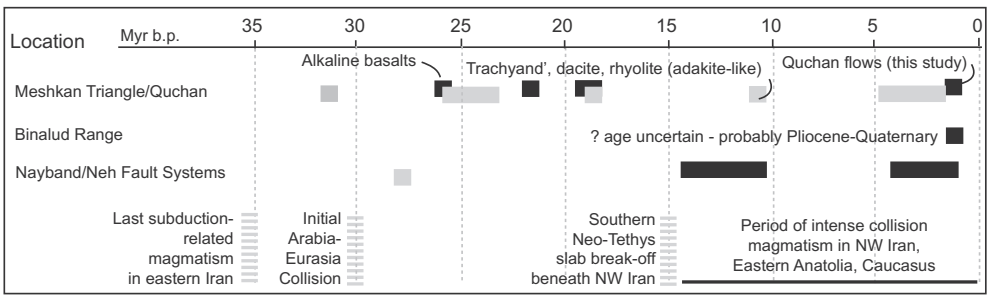

Fig. 2. Timeline showing dated magmatic events in Eastern Iran using K–Ar, Ar–Ar and relative dating discussed in Ghasemi et al. (2010), Shabanian et al. (2012), Walker et al. (2009), Pang et al. (2012) and Saadat and Stern (2012). Felsic samples are shown in grey, mafic in black.

3. Analytical methods

In addition to the previously published geochemical results from the Binalud Range and the Nayband and Neh Faults, which are discussed in subsequent sections, we present new analyses of ten mafic whole-rock samples from Quchan which were powdered by agate ball mill at Durham University. Major elements were analysed from fused glass beads using a PANalytical Axios Advanced X-ray Fluorescence (XRF) spectrometer at the University of Leicester. Leftover fractions were returned to Durham, digested using a standard HF-HNO_3 digestion technique and run on a Thermo X2 inductively-coupled plasma mass spectrometer (ICP-MS) at the Durham Geochemistry Centre (DGC) for trace elements. Data quality was monitored with blanks, multi-run and within-run duplicates, Re–Rh spikes, and five international reference standards. Standard W2 ($n = 23$) gave first relative standard deviations of 10% or better for all transition metals (excepting 11% for Cr), the large ion lithophile elements (LILE), high field strength elements (HFSE) and the rare earth elements (REE). Results are presented in Table 1.

Four Quchan samples were dissolved using standard HF-HNO_3 digestion in the DGC and underwent pre-concentration for radiogenic isotope analysis based on Dowall et al. (2007). Solutions were run through 1 ml pipettes containing Sr-spec resin to collect Sr- and Pb-bearing fractions. The high field strength element (HFSE)- and Rare Earth Element (REE)-bearing fraction was run through 10 ml polypropylene columns containing Bio-Rad AG50W-X8 200–400 mesh cation-exchange resin, with Nd collected as part of a general REE fraction. The HFSE-bearing fraction was run through 10 ml polypropylene columns containing Bio-Rad AG1-X8 anion-exchange resin to separate Hf from Ti. All samples were taken up in 400–500 μl of 3% HNO_3.

Radiogenic isotope analysis was conducted on a Thermo Neptune Multi-Collector ICP-MS at the DGC. Sr samples were tested for concentrations using ^{84}Sr before being diluted to produce an approximate ^{88}Sr beam of 20V. Sr was run with international reference standard NBS987 giving a mean $^{87}Sr/^{86}Sr$ of 0.710279 ± 0.000019 (2σ, $n = 12$, uncertainty = 27.2 ppm). Results were normalised to $^{87}Sr/^{86}Sr = 0.710240$. Nd was run with J&M and Sm-doped J&M standards giving a mean $^{143}Nd/^{144}Nd$ of 0.511106 ± 0.000014 (2σ, $n = 19$, uncertainty = 26.9 ppm). Results were normalised to $^{143}Nd/^{144}Nd = 0.511110$. Pb samples were spiked with a Tl solution giving a Pb/Tl ratio of ~12 to minimise overlap of tails of ^{205}Tl onto ^{204}Pb, and ^{206}Pb onto ^{205}Tl. Pb was run with standard NBS981 and results corrected offline for mass bias using the $^{205}Tl/^{203}Tl$ ratio of the Tl spike. A $^{205}Tl/^{203}Tl$ ratio of 2.388770 used to correct Pb isotope ratios, which was calculated by minimising the difference between the average of Pb isotope ratios for that session and the preferred values of Galer (1997) for NBS981. Final values and absolute errors for NBS981 were: $^{206}Pb/^{204}Pb = 16.94044 \pm 0.00082$; $^{207}Pb/^{204}Pb = 15.49757 \pm 0.00120$ and $^{208}Pb/^{204}Pb = 36.71486 \pm 0.00376$ (2σ, $n = 10$). The Hf samples were run with standard JMC475 giving a mean $^{176}Hf/^{177}Hf$ of 0.282157 ± 0.000010 (2σ, $n = 9$, uncertainty = 36.9 ppm). Results were normalised to $^{176}Hf/^{177}Hf = 0.282160$.

4. Geochemical results from Quchan and comparison with other Eastern Iranian centres

4.1. Major and trace elements

4.1.1. Quchan

The mafic samples analysed from Quchan for this study are rather homogeneous in major element composition, with 47–49 wt.% SiO_2, MgO ranging from 7 to 9 wt.% and Mg# from 54 to 59 (Table 1). The lavas are classified mostly as trachy-basalts with one sample falling in the basanite field in Fig. 3a. The samples are sodic ($Na_2O/K_2O = 2–3$), although they fall in the high-K to shoshonitic categories in Fig. 3b. Samples have reasonably high TiO_2 (2.2–2.3 wt.%) and moderate Al_2O_3 concentrations (~14 wt.%) (Table 1).

The Quchan samples have low Sc concentrations (~15 ppm) and slightly higher Cr relative to Ni (~180 ppm vs. 140 ppm). Of the large ion lithophile elements (LILE), Sr ranges from 700 to 1400 ppm, Ba from 750 to 850 ppm and Rb from 15 to 85 ppm – large ranges which do not correlate systematically with loss-on-ignition values (Table 1). On a chondrite-normalised rare earth element (CN-REE) plot, samples follow very similar patterns to one another, with LREE/HREE (light/heavy REE) enrichment and La/Yb_{CN} of ~14–17 (Fig. 4a). REE patterns have consistent slopes with fractionated HREE (Dy–Yb) and no Eu anomalies. The primitive mantle-normalised (PMN) trace element plot shows that samples have either positive or negative Rb spikes (Fig. 4b). Samples have large positive Nb–Ta anomalies, depletion in K and small negative Ti and P anomalies. Depletion and fractionation of the HREE is very marked on this plot.

4.1.2. Other Eastern Iranian Late Cenozoic centres

Samples previously analysed from the Binalud Range by Saadat and Stern (2012) are slightly more alkalic than the rocks from Quchan, plotting mostly as phono-tephrites (Fig. 3a), and they have lower MgO contents on average compared with the Quchan samples (Table 1). The rocks from the Nayband/Neh region are considerably more heterogeneous. The least evolved samples include basalts, trachy-basalts and basanites. SiO_2 concentrations reach up to 53 wt.%, however, with the majority of samples plotting as basaltic trachy-andesites (Fig. 3a). The Nayband/Neh samples also appear to evolve from shoshonitic to medium-K compositions (Walker et al., 2009; Saadat et al., 2010; Pang et al., 2012) (Table 1; Fig. 3b).

The Binalud rocks display very similar concentrations of most trace elements to the Quchan samples, and have nearly identical REE and PMN trace element plots. The Nayband/Neh samples have a similar PMN trace element profile to the other locations but with a much wider range of trace element concentrations (Fig. 4b). Around half of the Nayband/Neh samples also have low Nb–Ta concentrations relative to the LREE and LILE, resulting in La/Nb ratios of >1 (Table 1). Samples are compared with the average OIB value (Sun and McDonough, 1989), showing that the Iranian rocks have similar shapes of pattern, albeit at slightly lower REE concentrations (Fig. 4a) and with more variable ('spikier') LILE patterns (Fig. 4b).

4.2. Radiogenic isotopes

4.2.1. Quchan

The Quchan mafic samples are isotopically homogeneous and have moderately radiogenic $^{87}Sr/^{86}Sr_{meas}$ of 0.7045–7051 and slightly enriched $^{143}Nd/^{144}Nd$ of ~0.5128 relative to bulk earth giving positive εNd_{meas} values of +2.7–3.3 (Table 2). Samples lie within and slightly to the right of the mantle array in Fig. 5, between depleted mantle and older crustal components (or the EMII end member). We can only compare whole rock $^{176}Hf/^{177}Hf$ ratios for Quchan with non-radiogenic (−ve εHf) ~11 Ma lamprophyres derived from a subduction-modified source close to the Zagros suture in NW Iran (Pang et al., 2013) and ~2.5 Ma alkali basalts in Armenia which have higher +ve εHf values compared to Quchan (Neill et al., in press) (Fig. 6a). Samples from Quchan lie on the terrestrial array in Fig. 6a and are more radiogenic than Bulk Earth, but less radiogenic than samples derived from the subduction-modified lithosphere beneath Armenia (Neill et al., in press), and also less radiogenic than typical Indian or

Table 1
Major and trace element compositions of Late Cenozoic mafic volcanic rocks from Quchan, NE Iran. LOI = loss-on-ignition. Average values are also provided for mafic rocks from the Binalud Range (Saadat and Stern, 2012; $n = 5$) and the Nayband/Neh faults in southeastern Iran (Walker et al., 2009; Saadat et al., 2010; Pang et al., 2012; $n = 29$).

	Q111	Q112	Q113	Q115	Q116	Q117	Q120	Q122	Q123	Q124	Binalud Range	Nayband-Neh
Easting	58 4 38.5	58 4 35.8	58 4 50.7	58 4 51.9	58 4 51.9	58 4 51.9	58 4 53.3	58 5 50.6	58 5 52.1	58 5 59.0	Average	Average
Northing	37 8 4.2	37 8 2.6	37 8 9.4	37 8 9.8	37 8 9.8	37 8 9.8	37 8 23.7	37 8 44.8	37 8 46.4	37 8 49.6	Values	Values
Type	Trachy-basalt						Basanite	Trachy-basalt			Basanite	Trach-bas
SiO_2	48.69	49.25	47.81	48.34	48.12	48.75	47.03	48.69	47.27	47.46	49.34	50.61
TiO_2	2.23	2.25	2.32	2.17	2.31	2.23	2.28	2.26	2.21	2.19	2.02	2.16
Al_2O_3	14.35	14.41	14.31	14.13	14.28	14.43	14.18	14.27	13.97	14.00	17.24	14.99
Fe_2O_3(t)	10.09	10.25	10.45	9.94	10.44	10.11	10.30	10.33	10.19	10.09	12.11	9.38
MgO	6.95	6.85	6.98	6.91	7.07	6.84	7.40	6.80	7.34	8.05	5.12	5.49
MnO	0.14	0.14	0.14	0.14	0.14	0.14	0.14	0.13	0.14	0.14	0.20	0.13
CaO	8.84	8.14	8.80	8.98	8.55	8.65	9.12	8.62	9.05	8.31	5.74	8.53
Na_2O	4.71	4.71	3.82	4.57	4.36	4.69	4.67	3.44	4.31	4.08	5.34	4.64
K_2O	1.67	1.72	1.37	1.85	1.50	2.09	1.58	1.90	1.49	1.68	2.22	1.40
P_2O_5	0.69	0.69	0.79	0.67	0.79	0.68	0.77	0.74	0.71	0.69	0.38	0.74
LOI	1.56	1.38	2.91	1.91	2.30	1.23	2.42	2.57	2.77	3.33	n/a	
Total	99.91	99.77	99.69	99.61	99.86	99.84	99.90	99.76	99.48	100.03		
Mg#	55	54	54	55	55	55	56	54	56	59	45	54
Sc	14.9	15.3	14.8	15.0	15.1	15.5	14.7	14.6	14.9	14.6		22.0
V	192	200	188	189	189	195	179	182	179	173	165	177
Cr	185	188	184	176	187	185	179	183	187	184	66	163
Co	37.5	39.3	37.6	37.5	38.0	38.7	38.4	34.9	38.3	37.0	n/a	29.4
Ni	133	145	138	137	157	135	136	145	144	139	97	85
Rb	15.4	14.8	86.3	15.9	75.2	20.6	43.4	38.7	55.8	42.9	43.2	28.4
Sr	730	733	1098	710	796	718	977	1399	1128	883	681	1095
Y	22.0	23.1	22.7	22.2	23.3	22.5	22.8	22.4	22.3	22.1	17.4	20.6
Zr	193.0	198.5	205.5	190.1	204.8	196.0	203.5	197.7	199.0	193.2	214.4	215.9
Nb	67.0	67.3	77.1	66.8	77.4	68.4	77.6	72.5	72.6	70.2	46.0	35.1
Ba	797	762	787	770	794	800	831	777	794	765	578	394
Hf	4.7	4.6	4.8	4.7	4.9	4.7	5.0	4.8	4.8	4.7	5.1	4.8
Ta	3.9	3.7	4.4	3.8	4.3	3.9	4.4	4.0	4.1	3.9	3.2	1.6
Pb	3.1	3.0	3.2	3.1	3.1	3.1	3.2	3.1	3.1	3.1	n/a	5.4
Th	4.3	4.2	4.5	4.3	4.5	4.1	4.5	4.3	4.3	4.2	3.2	4.5
U	1.2	1.3	1.3	1.2	1.3	1.1	1.2	1.8	1.4	1.0	1.0	0.7
La	31.9	32.9	36.0	33.0	36.2	32.7	36.4	34.6	34.9	33.8	21.8	34.9
Ce	63.0	63.2	69.8	64.1	71.4	64.4	73.0	67.5	68.3	67.5	45.2	74.5
Pr	8.7	8.6	9.6	8.7	9.7	8.7	10.0	9.3	9.3	9.3	5.9	11.6
Nd	34.9	34.7	38.5	35.6	38.6	35.6	40.4	37.2	37.8	37.0	24	37.1
Sm	7.1	7.0	7.7	7.3	7.8	7.3	8.0	7.4	7.6	7.6	5.3	7.6
Eu	2.2	2.2	2.4	2.2	2.4	2.2	2.5	2.3	2.4	2.3	1.8	2.1
Gd	6.7	6.8	7.2	6.9	7.2	6.9	7.7	7.2	7.4	7.2	5.8	6.4
Tb	0.9	0.9	1.0	0.9	1.0	0.9	1.0	0.9	1.0	0.9	0.7	0.9
Dy	4.6	4.6	4.8	4.6	4.8	4.7	5.0	4.8	4.8	4.7	n/a	4.1
Ho	0.8	0.8	0.8	0.8	0.8	0.8	0.8	0.8	0.8	0.8		0.7
Er	1.9	1.9	1.9	1.9	1.9	1.9	1.9	1.9	1.9	1.8		1.8
Tm	0.3	0.3	0.3	0.3	0.3	0.3	0.3	0.3	0.3	0.3		0.2
Yb	1.5	1.4	1.4	1.5	1.4	1.5	1.5	1.5	1.5	1.4	1.4	1.4
Lu	0.2	0.2	0.2	0.2	0.2	0.2	0.2	0.2	0.2	0.2	0.2	0.2

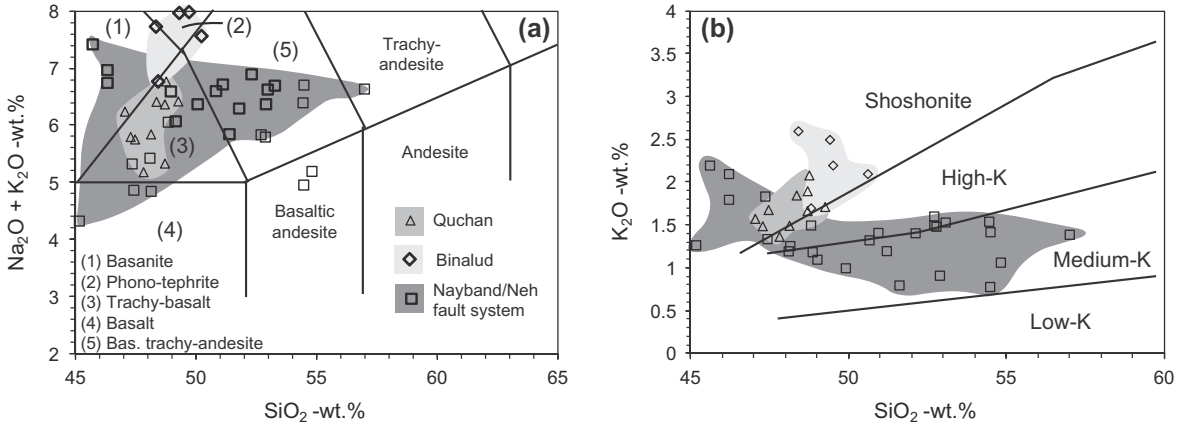

Fig. 3. (a) TAS classification diagram for the Late Cenozoic mafic rocks of Eastern Iran after Le Maitre et al. (2002). (b) K_2O vs. SiO_2 classification diagram after Peccerillo and Taylor (1976). Binalud and Nayband/Neh data from Walker et al. (2009), Saadat et al. (2010), Pang et al. (2012) and Saadat and Stern (2012).

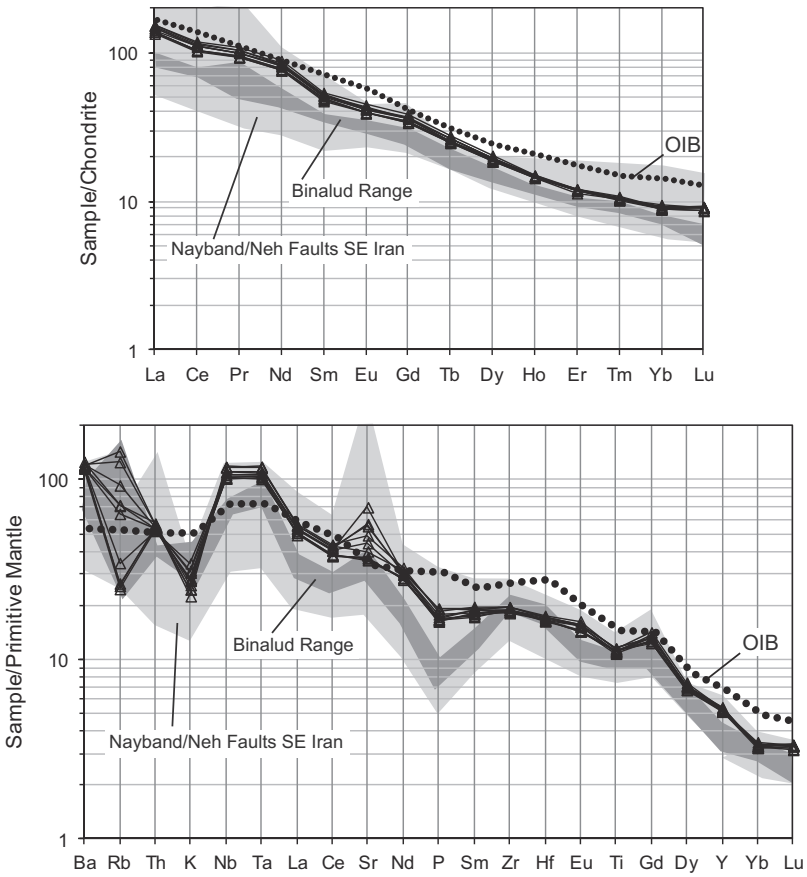

Fig. 4. (a) Chondrite-normalised REE concentrations for the Quchan lavas (triangles), with normalisation after McDonough and Sun (1995). (b) Primitive mantle-normalised trace element plot with normalisation after Sun and McDonough (1989). Source of Binalud and Nayband/Neh data as per Fig. 3.

Atlantic Ocean MORB. Samples fall between the EMII end member and depleted (Atlantic) MORB. Pb isotope ratios for Quchan lie above the Northern Hemisphere Reference Line in Fig. 6c and d and again lie between DMM (Depleted MORB Mantle) and the EMII end member.

4.2.2. Other Eastern Iranian Late Cenozoic centres

Sr–Nd and some Pb isotopic data are available in the literature for the Binalud (Saadat and Stern, 2012) and Nayband/Neh basalts (Saadat et al., 2010; Pang et al., 2012). The two Binalud samples have slightly lower $^{143}Nd/^{144}Nd$ compared to Quchan (Fig. 5), and noticeably lower Pb isotope ratios (Table 2; Fig. 6b and c). Samples from the Nayband/Neh region (Saadat et al., 2010; Pang et al., 2012) are more isotopically variable than those from the other locations; perhaps as a function of the larger number of analyses, although Walker et al. (2009) concluded that these samples had experienced crustal contamination. Consequently, although many of the samples display similar Nd–Sr isotope characteristics to the Quchan samples, a number of Nayband/Neh rocks have considerably higher $^{87}Sr/^{86}Sr$ (Fig. 5). The few Nayband/Neh samples to be analysed for Pb isotopes have ratios similar to the Binalud samples, but a couple have slightly higher $^{206}Pb/^{204}Pb$ (Table 2; Fig. 6b and c).

5. Discussion

5.1. Magmatic differentiation

Because many of the analysed rocks were erupted at different times over a period of at least 14 Myr, with many flows and cones remaining undated, a quantitative assessment of differentiation processes is impossible. Furthermore, most sites have only a few analyses available. Nevertheless, some general geochemical patterns are observed, and these allow us to qualitatively consider contamination and fractionation processes affecting the Eastern Iranian mafic samples.

5.1.1. Crustal contamination

La/Nb ratios in mantle-derived rocks are sensitive to crustal contamination given the high LREE/HFSE characteristics of typical continental crust (Taylor and McLennan, 1985). Fig. 7a shows La/Nb relative to SiO_2 with the latter used as an index of magmatic differentiation. The new Quchan samples as well as most of the previously-analysed Binalud and roughly half the Nayband/Neh rocks display little or no variation in La/Nb ratios with increasing SiO_2, which is an indication of fractionation of phases with similar La and Nb partitioning behaviour (e.g., olivine, pyroxene). The remaining Nayband/Neh samples define a trend of increasing La/Nb with respect to SiO_2 which can be attributed to assimilation of high-La/Nb crustal contaminants during magma evolution (Walker et al., 2009). Given the enrichment of Th and other LILE in the continental crust (Taylor and McLennan, 1985), the sharp increase in Th/Yb ratios relative to SiO_2 again in about half the Nayband/Neh samples, can be attributed to crustal contamination (Fig. 7b). The remaining samples show no increase in Th/Yb relative to SiO_2 and again can be argued to have evolved mostly by fractional crystallisation. All of the low Th/Yb samples fall within the MORB-OIB array in Th/Yb vs. Nb/Yb space (Fig. 7c) and also 'trend back' to La/Nb ratios of ~1 or less (Fig. 7a).

Table 2
Measured radiogenic isotope results for mafic collision magmas of NE Iran. Epsilon values are calculated for the present day using $(^{143}Nd/^{144}Nd)_{CHUR} = 0.512638$ and $^{176}Hf/^{177}Hf = 0.282772$ for chondritic Earth. Published values for the Binalud and Nayband/Neh areas are from Saadat et al. (2010), Saadat and Stern (2012) and Pang et al. (2012) for comparison. Epsilon values from Pang et al. (2012) (sample AV-NEH onwards) are age-corrected based on Ar–Ar dating results. n/a = not available.

	$^{87}Sr/^{86}Sr$	$\pm2\sigma$	$^{143}Nd/^{144}Nd$	$\pm2\sigma$	εNd	$^{176}Hf/^{177}Hf$	$\pm2\sigma$	εHf	$^{206}Pb/^{204}Pb$	$\pm2\sigma$	$^{207}Pb/^{204}Pb$	$\pm2\sigma$	$^{208}Pb/^{204}Pb$	$\pm2\sigma$
Quchan														
Q111	0.704712	0.000016	0.512783	0.000013	2.83				18.66859	0.00223	15.60319	0.00232	38.82987	0.00729
Q115	0.704741	0.000018	0.512774	0.000008	2.65	0.282952	0.000007	6.37	18.70380	0.00154	15.60460	0.00159	38.87996	0.00481
Q116	0.704528	0.000018	0.512809	0.000006	3.33	0.282969	0.000006	6.97	18.68160	0.00180	15.59654	0.00198	38.84880	0.00545
Q120	0.705105	0.000016	0.512808	0.000011	3.31	0.282979	0.000003	7.32	18.6741	0.00154	15.59744	0.00153	38.85264	0.00434
Binalud														
NE1	0.705250	n/a	0.512738	n/a	2.0				18.53	n/a	15.54	n/a	38.44	n/a
NE2	0.705013	n/a	0.512735	n/a	1.9				18.44	n/a	15.53	n/a	38.13	n/a
Nayband/Neh Fault systems														
S2–3	0.705555	n/a	0.512728	n/a	1.76				18.470	n/a	15.556	n/a	38.409	n/a
S3–1	0.705312	n/a	0.512686	n/a	0.94				18.570	n/a	15.581	n/a	38.589	n/a
A-29	0.705774	n/a	0.512707	n/a	1.34									
D-23	0.705298	n/a	0.512686	n/a	0.94									
D-16	0.705777	n/a	0.512709	n/a	1.32									
D-21	0.705291	n/a	0.512688	n/a	0.91									
GM-1	0.704592	n/a	0.512709	n/a	1.39				18.755	n/a	15.583	n/a	38.753	n/a
GG-1	0.704505	n/a	0.512730	n/a	1.79				18.975	n/a	15.596	n/a	38.596	n/a
AV-NEH	0.704868	0.000011	0.512813	0.000004	3.4									
BV-NEH	0.705015	0.000003	0.512775	0.000003	2.7									
CV-NEH	0.707253	0.000008	0.512768	0.000002	2.6									
1	0.705113	0.000009	0.512775	0.000002	2.7									
2	0.705545	0.000009	0.512800	0.000006	3.2									
3	0.704954	0.000005	0.512823	0.000001	3.6									
Z-BKH-1	0.704879	0.000002	0.512813	0.000002	3.5									
Z-BKH-2	0.705896	0.000005	0.512793	0.000002	3.1									
Z-B-1–85	0.705020	0.000011	0.512779	0.000007	2.9									
Z-B-2–85	0.704870	0.000012	0.512794	0.000004	3.1									
Z-50–85	0.704786	0.000010	0.512806	0.000005	3.4									
08–06	0.705453	0.000013	0.512706	0.000013	1.4									
08–07	0.706524	0.000007	0.512718	0.000001	1.6									
08–112	0.704747	0.000006	0.512795	0.000004	3.1									
10–08	0.704737	0.000006	0.512787	0.000003	3.0									
10–10	0.705831	0.000006	0.512767	0.000002	2.6									
10–14	0.705486	0.000006	0.512706	0.000004	1.4									

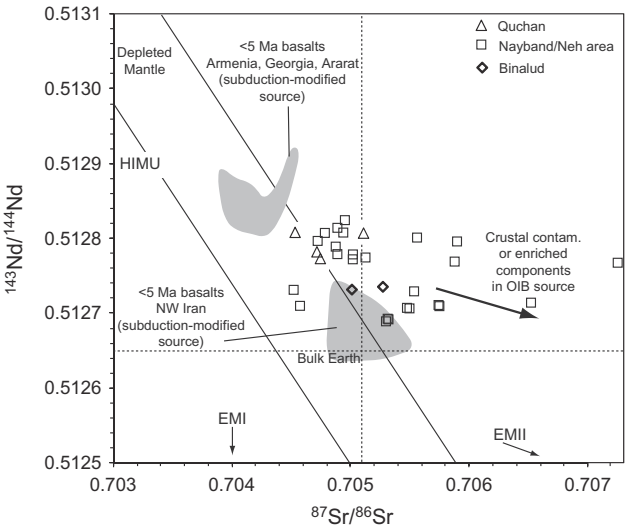

Fig. 5. Nd–Sr isotope composition of samples from Quchan (this study), Binalud (Saadat and Stern, 2012), the Nayband/Neh Fault system (Saadat and Stern, 2010; Pang et al., 2012), and compilations from NW Iran (Kheirkhah et al., 2013) and selected subduction-modified centres in the Caucasus and Eastern Anatolia (Neill et al., 2013a).

There does not appear to be a geographic trend to the interpreted contamination. Fig. 7a and b show significant overlap in La/Nb and Th/Yb ratios between samples from the Nayband and Neh Fault systems. There is also a distinct lack of correlation between $^{87}Sr/^{86}Sr$ isotope characteristics and La/Nb and Th/Yb ratios, such that a single high-$^{87}Sr/^{86}Sr$ contaminant is not clearly responsible for trace element variation (Fig. 8). Neill et al. (2013a) pointed out that lavas in the northern part of the Arabia–Eurasia collision zone in Armenia may have been contaminated by either Gondwanaland-related terranes or more Mesozoic–Paleogene Tethyan arc crust. The same may be true for the Nayband/Neh samples: low-$^{87}Sr/^{86}Sr$ samples with high Th/Yb–La/Nb characteristics may be contaminated by isotopically depleted Tethyan arc lithologies, whereas those with higher $^{87}Sr/^{86}Sr$ may have been influenced by older Cimmerian basement or arc rocks with high $^{87}Sr/^{86}Sr$ values. Furthermore, a range in $^{87}Sr/^{86}Sr$ is observed in the low-Th/Yb–La/Nb samples (Fig. 8a and b) which may relate to compositional heterogeneities in the mantle source (see Section 5.2).

5.1.2. Fractional crystallisation

We observe low MgO contents (<7 wt.%) in all of the samples, demonstrating that they are not close to being primary magmas, and may have experienced fractionation of mafic minerals such as olivine and pyroxene, consistent with the observed phenocryst assemblages. A lack of Eu anomalies (Fig. 4a) and the fact that many of the samples have elevated concentrations of Ba and Sr relative to average OIB (Sun and McDonough, 1989) (Fig. 7d) may be at least partly attributed to incompatible behaviour of these elements during fractionation of olivine and pyroxenes and to limited feldspar fractionation during magma evolution.

5.2. Mantle source characteristics

5.2.1. Elemental evidence

As the samples from each locality appear to be associated with low-SiO_2 parental magmas with low La/Nb and Th/Yb, they are unlikely to have a subduction-modified mantle source (Fig. 7a and b). On Fig. 7c, all of the non-contaminated samples have high Nb/Yb ratios relative to Th/Yb, such that they plot at the enriched end of the mantle array. High HFSE/HREE ratios indicate an incompatible element-enriched mantle source and/or small degrees of partial melting. This pattern is common to OIB in general and also to high-Nb basalts which are often found in subduction settings (e.g., Castillo et al., 2002; Sorbadere et al., 2013; Neill et al., 2013b). Further evidence of an OIB-like enriched source comes from the lack of negative HFSE anomalies for most samples on the PM-normalised trace element plot (Fig. 4b).

Although OIB-like rocks can be generated in subduction settings by melting amphibole- or rutile-bearing HFSE-enriched sources (Hastie et al., 2011; Allen et al., 2013a), there is no evidence for subducted sediment-related fluid activity, especially as the samples have modest Th/La ratios of ~0.12 (Plank, 2005) and no Ce anomalies on the normalised plots (Fig. 4a; Hastie et al., 2013). Most studies agree that these rocks form by low-degree melting of enriched asthenospheric mantle (e.g., Macpherson et al., 2010). An alternative model is that melts are formed in the lithospheric mantle, but that the mantle source was enriched by small-volume melts derived from the convecting asthenosphere (e.g., Ekici et al., 2014). Previous workers have stated that the Eastern Iranian OIB-like rocks formed by melting of the convecting asthenosphere (Pang et al., 2012; Saadat and Stern, 2012; Su et al., 2014) although this information needs to be reconciled with geophysical and xenolith-based evidence for lithospheric thickness (see Section 6.2).

Another conclusion from elemental analyses is that carbonate metasomatism in the mantle source is not responsible for the high Ba–Sr character of these samples (Fig. 7d). Most basaltic rocks derived from carbonated mantle sources, such as the basanite–tephrite volcanics at Qa'le Hasan Ali on the southern Nayband Fault (Saadat and Stern, 2014), have low SiO_2, Zr and Hf as well as high CaO, Zr/Hf and low Ti/Eu (Ionov et al., 1993; Rudnick et al., 1993). This description is at odds with the low-CaO, high-Zr signature of our samples (Table 1). Modest K_2O values of <1.5 wt.% are also inconsistent with the presence of significant amounts of hydrous phases (e.g., phlogopite) in the mantle source. Although the samples have quite low CaO and Sc concentrations, they do not have high SiO_2 or low Ni (Table 1), so these features are likely to relate to fractionation of pyroxene rather than providing definite evidence for a pyroxenitic source (e.g., Sobolev et al., 2005). Finally, the moderate to low Y (<25 ppm) and low HREE concentrations (Yb < 2 ppm), along with fractionated HREE patterns ($Dy/Yb_{CN} > 1$) in all mafic suites (Fig. 4a) indicate that garnet was likely to have been involved as a residual phase at some point during partial melting processes. Overall, we favour an anhydrous, incompatible element-enriched garnet peridotite source for OIB-type magmatism.

5.2.2. Isotope evidence

Our new isotope data, coupled with that published by Saadat et al. (2010), Saadat and Stern (2012) and Pang et al. (2012) demonstrates that the source of the East Iranian basalts is moderately isotopically enriched and unlike 'typical' depleted mantle. The much-debated DUPAL mantle (Dupré and Allègre, 1983; Hart, 1984), common to some Tethyan ophiolites (e.g., Liu et al., 2014) and almost ubiquitous in the modern Indian Ocean (e.g., Ingle et al., 2003; Meyzen et al., 2005) is not an obvious source for the 'enriched' signature of the East Iranian basalts either. Firstly, DUPAL basalts typically have very high εHf for a given εNd (Ingle et al., 2003). The Quchan samples lie on the terrestrial array in Hf–Nd space and are not particularly close to Indian MORB values (Fig. 6a). Secondly, DUPAL basalts were originally defined as having high $^{208}Pb/^{204}Pb$ and $^{87}Sr/^{86}Sr$ but low $^{206}Pb/^{204}Pb$ (Dupré and Allègre, 1983). Instead, our samples do not have low $^{206}Pb/^{204}Pb$, nor do they have especially high $^{208}Pb/^{204}Pb$ (Fig. 6b and c).

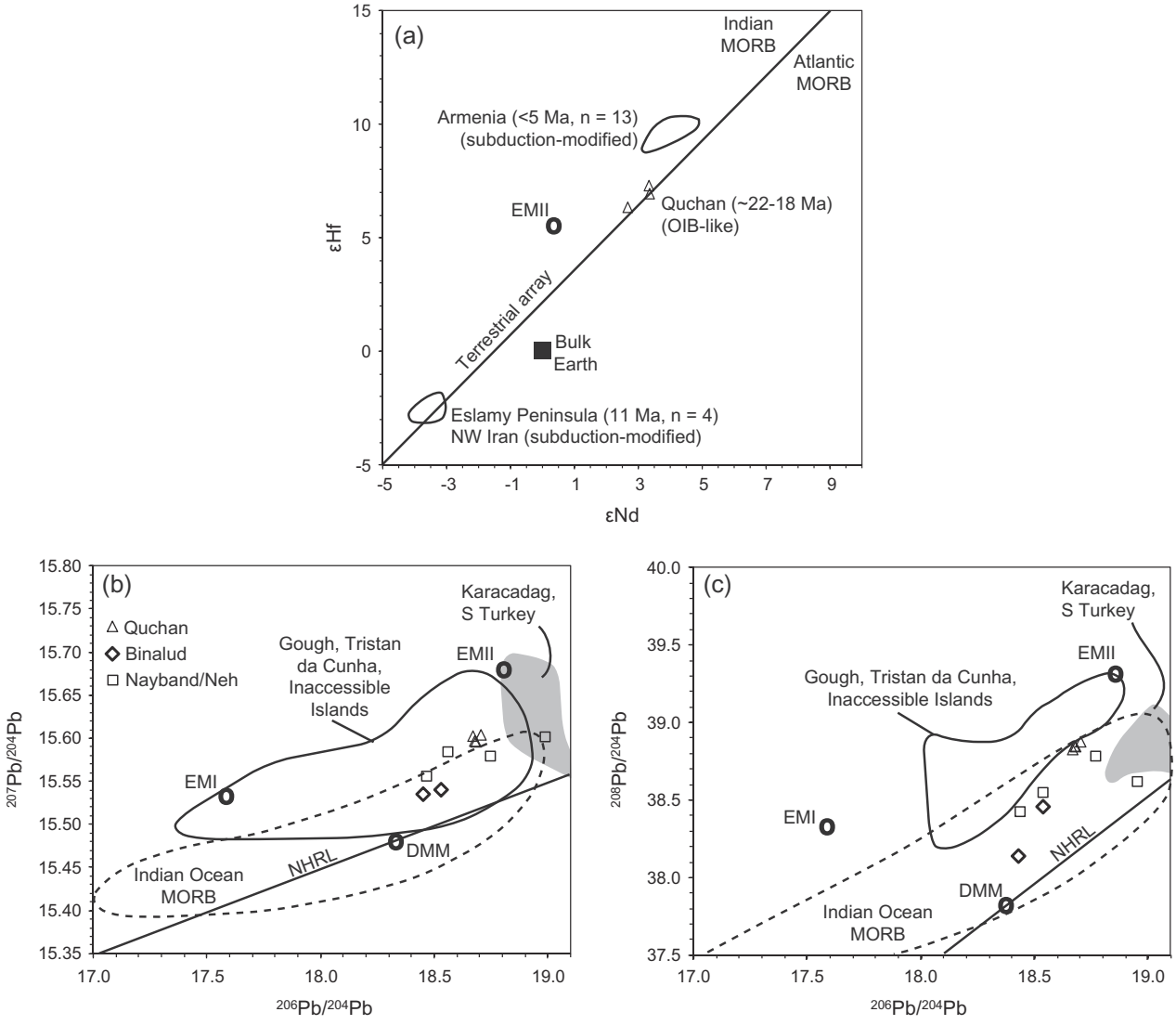

Fig. 6. Measured isotopic composition of the Quchan lavas compared with selected recent lavas in the region. (a) $^{176}Hf/^{177}Hf$ vs. $^{143}Nd/^{144}Nd$. Eslamy samples from Pang et al. (2013); Armenian samples from Neill et al. (in press). Terrestrial Array from Chauvel et al. (2008). EMII from Nowell et al. (1998). (b) $^{207}Pb/^{204}Pb$ vs. $^{206}Pb/^{204}Pb$ and (c) $^{208}Pb/^{204}Pb$ vs. $^{206}Pb/^{204}Pb$. NHRL (Northern Hemisphere Reference Line) and Indian Ocean Mantle from Saal et al. (2005). Karacadag (Ekici et al., 2014) is an OIB-type volcano in S Turkey on the Arabian Plate and appears to be derived at least in part from an asthenospheric source which is nevertheless more enriched than the Iranian samples. Suphan volcano in Eastern Anatolia (Özdemir and Güleç, 2014), which has been argued to have mixed with asthenospheric components, falls around the EMII end member on Pb isotope plots so is not plotted here. Samples are compared to similar oceanic basalts from Gough, Tristan da Cunha and Inaccessible Islands, as compiled in Gibson et al. (2005).

As shown in Fig. 8, there are a variety of $^{87}Sr/^{86}Sr$ ratios associated with the low Th/Yb and La/Nb samples which may reflect source isotopic heterogeneity rather than crustal contamination. We note that the samples for which there are Pb isotope analyses all have La/Nb < 0.63 and Th/Yb < 3.7 (Saadat and Stern, 2012; Saadat et al., 2010; this study) which appears to rule out crustal contamination as a cause of the moderately high ^{207}Pb and ^{208}Pb values already described.

The precise nature of the mantle source(s) is difficult to assess isotopically given the lack of samples. One possibility is that there has been straightforward mixing of depleted and EMII-like components which would explain why the samples sit between these end members in Fig. 6b and c. The absence of any trends towards high εHf or $^{208}Pb/^{204}Pb$ indicate that the depleted component is 'typical' DMM-like upper mantle. Few samples of intraplate rocks erupted through oceanic crust display Pb isotopes which lie directly between DMM and EMII. Such oceanic examples do not suffer from contamination effects, so may be compared with our samples for which contamination has already been ruled out. Most similar are the rocks of Gough and Tristan da Cunha Islands and Inaccessible Seamount in the South Atlantic (compilation in Gibson et al., 2005; Fig. 6b and c). Gibson et al. (2005) argued that the rather high ^{206}Pb, ^{207}Pb and ^{208}Pb isotope signatures displayed at these locations were due to incorporation of 10's of per cent American or African sub-continental lithosphere in the source. Our continental OIB-like samples may have a similar Pb isotope signature to these locations due to the magmas passing through similar mantle en route to the surface. Alternatively, the OIB-like samples may be derived at least in part from melting of delaminated sub-continental lithosphere (see Section 6).

5.3. Partial melting conditions

Partial melting models have already been run for mafic rocks in Eastern Iran. Walker et al. (2009) using trace element inversion to argue for the metasomatism of MORB-source mantle by very small

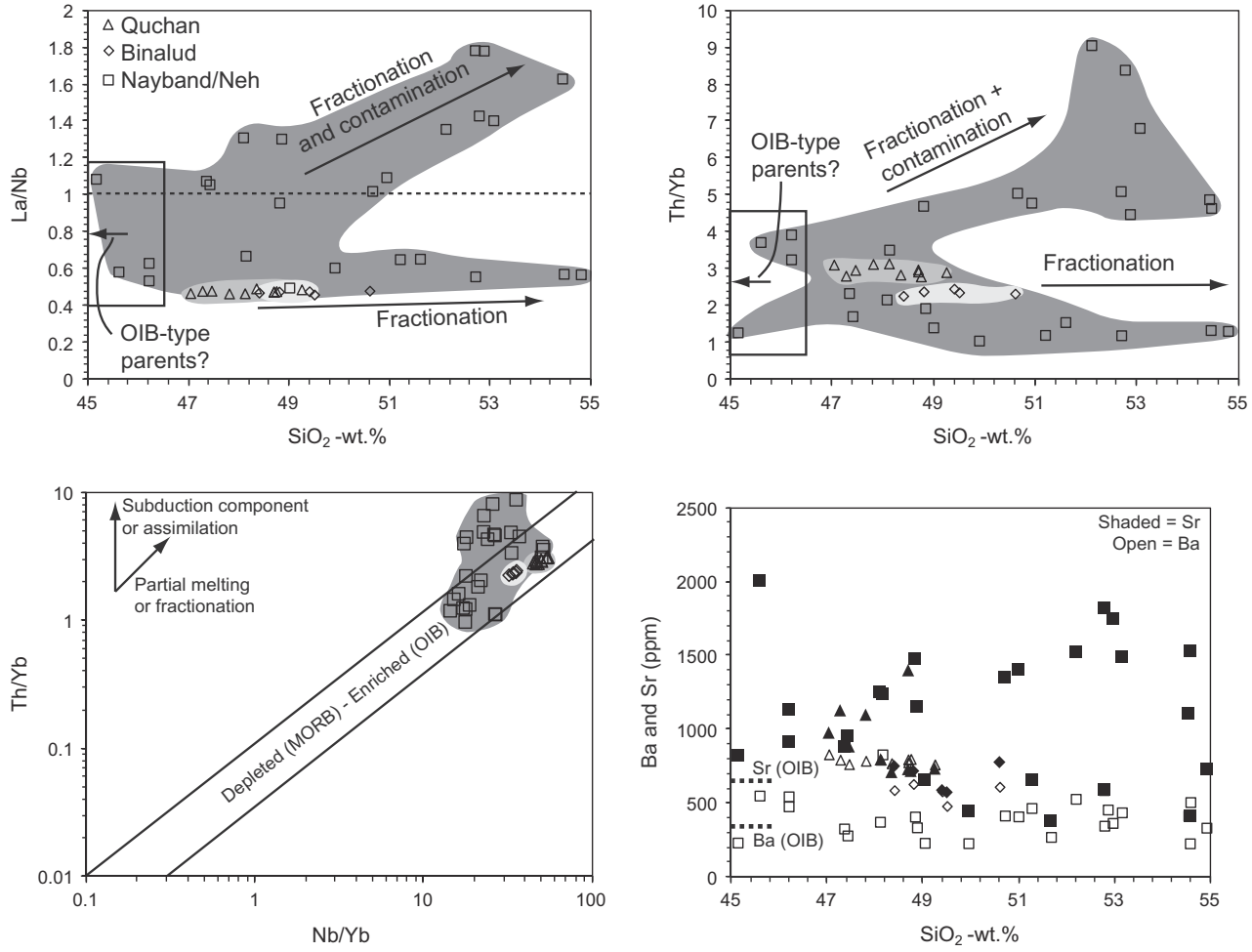

Fig. 7. Trace element variation plots to identify crustal contamination and fractionation effects. (a) La/Nb vs. SiO_2. (b) Th/Yb vs. SiO_2. (c) Th/Yb vs. Nb/Yb after Pearce and Peate (1995). (d) Ba and Sr vs. SiO_2 with OIB values from Sun and McDonough (1989).

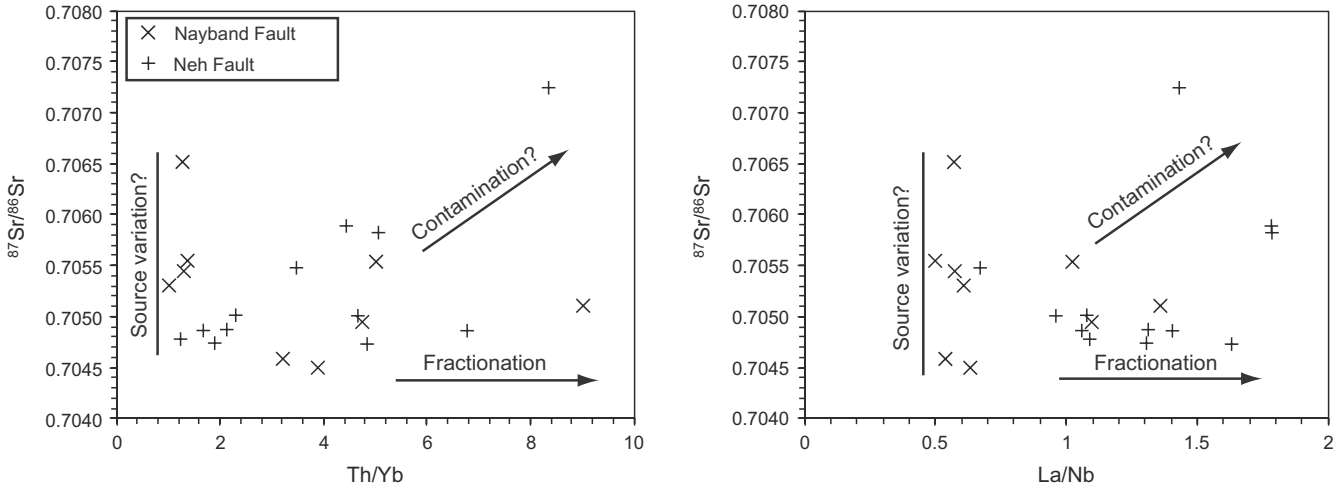

Fig. 8. (a) and (b) Plots of mafic samples of Saadat and Stern (2010) and Pang et al. (2012) from the Nayband and Neh Fault region showing limited correlation between contamination-sensitive Th/Yb-–La/Nb ratios and $^{87}Sr/^{86}Sr$. See text for discussion.

volume (F = ~0.5%) partial melts from the garnet stability field, followed by more extensive melting of the newly-metasomatised source in the spinel facies to generate the Nayband/Neh parental magmas. A similar process was argued for by Saadat and Stern (2012) for the Binalud alkali basalt cone, who used non-modal fractional melting equation to argue for mixing of ~0.5% melts of garnet-facies mantle with ~5% melts of a shallower spinel facies source, presumably within a single melting column in the

garnet–spinel transition zone. Pang et al. (2012) instead used non-modal batch melting equations to argue for a single stage process involving a more enriched mantle source undergoing ~3–10% melting in the garnet stability field. We have not attempted to add confusion by undertaking further modelling, particularly given the geochemical similarity between the least-contaminated Nayband/Neh samples, the Binalud rocks and our Quchan locality.

5.4. Relationship to felsic volcanic centres

A particularly puzzling aspect of the OIB-like mafic eruptions in Eastern Iran is that they are penecontemporaneous with adakite-like magmatic activity (Shabanian et al., 2012) (Figs. 2 and 9). Any petrogenetic model must therefore accommodate melting conditions suitable for the generation of adakite-like rocks (or a mafic precursor to adakitic magmas) and the OIB-like alkali basalts. "Adakite" is a term used to describe a huge variety of sodic felsic magmas, typically characterised by low MgO–Ni–Cr concentrations and high La/Yb and Sr/Y ratios (see Moyen, 2009 for discussion). They are considered to be the product of: (1) fusion of subducting slabs (Defant and Drummond, 1990); (2) fusion of existing or recently under-plated mafic lower crust (Atherton and Petford, 1993; Rapp and Watson, 1995); (3) differentiation of arc and/or arc-like magmas involving M-HREE-compatible fractionating phases such as garnet and amphibole, (Macpherson et al., 2006); possibly combined with (4) suppressed plagioclase fractionation at high ρH_2O (Richards et al., 2012) to produce high Sr/Y ratios. The Late Cenozoic felsic rocks in Eastern Iran are dome-forming trachy-andesites, dacites and rhyolites which do display adakite-like trace element signatures and also small to moderate negative HFSE anomalies (Nb–Ta, Ti) (Shabanian et al., 2012) (Fig. 9a–d).

Since subduction processes ended in the Eocene, slab melting is an extremely unlikely option for Late Cenozoic adakite petrogenesis. Melting of the lowermost Tethyan arc crust beneath northeast Iran has been favoured by Shabanian et al. (2012). Based on waveform tomography, the crust in the region of the Meshkan Triangle is presently ~40–50 km thick (Manaman et al., 2011; Motaghi et al., 2012; in press). P–T estimates obtained from the spinel peridotite xenoliths in the Binalud cone indicate mantle temperatures of 966–1069 °C, assuming equilibration at 1.5 GPa (45 km). Su et al. (2014) contended that the gabbroic xenoliths reported by Saadat and Stern (2012) from the Binalud cone stabilised at ~9 kbar (~30 km) and ~875 °C. These conditions provided an approximate geotherm indicating near-present-day temperatures at the base of 42 km thick crust of ~980 °C. Using the experimental data of Rapp and Watson (1995), these temperatures and pressures exceed the solidus for both H_2O-saturated and under-saturated meta-basalts, but with amphibole and plagioclase stabilised in the residue. Melts of such rock types should be low in Sr and Al (e.g., Hastie et al., 2010), which is not the signature of the Meshkan adakite-like rocks as they have high Al_2O_3 of 16–20 wt.% and Sr ranging from 270 to 710 ppm (Shabanian et al., 2012). On these grounds, crustal melting may not be an appropriate model for the genesis of the Meshkan adakite-like rocks. The timing of crustal thickening in the region during the Late Cenozoic is not certain but even thinner crust (<30 km) would still produce melts with amphibole and plagioclase in the residue (Rapp and Watson, 1995).

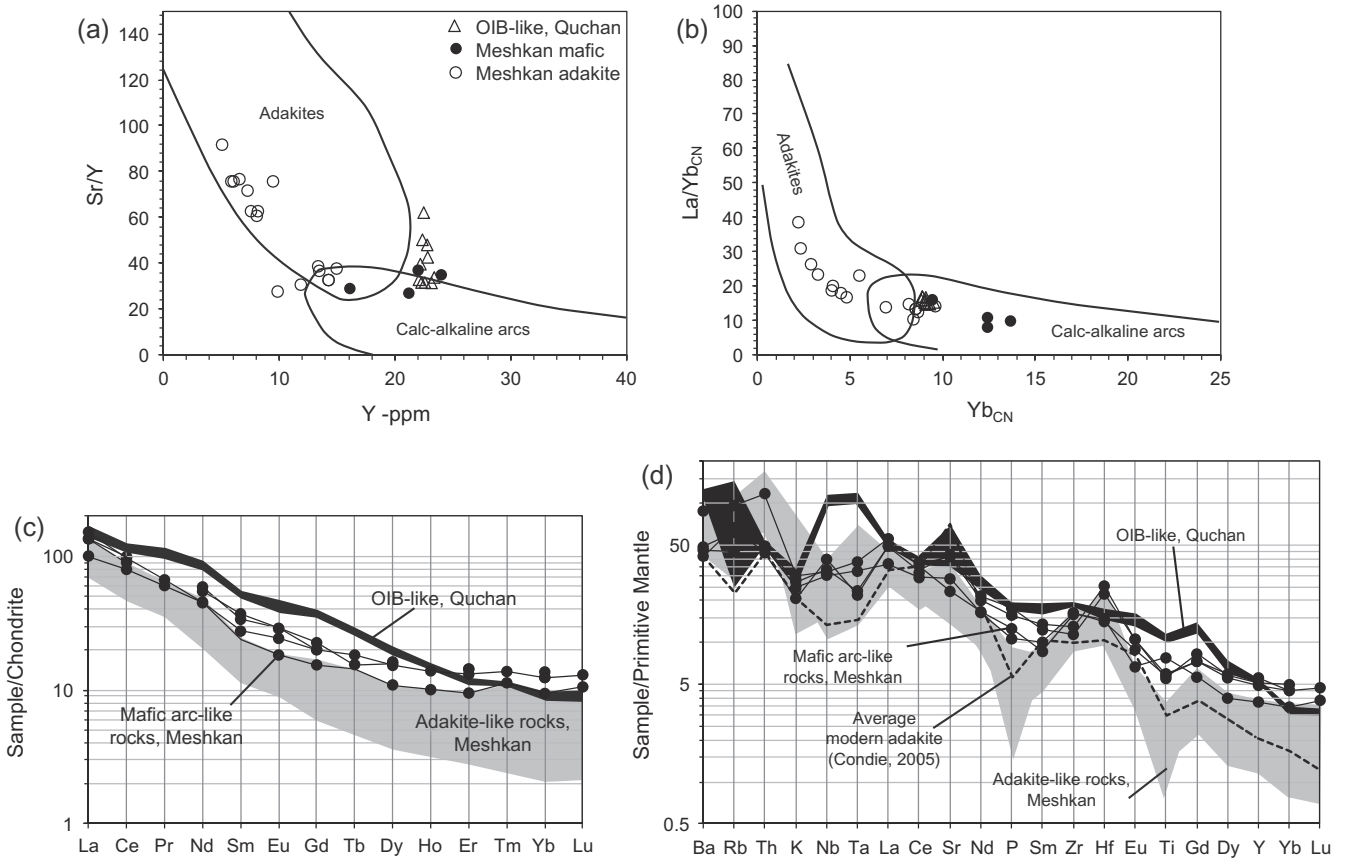

Fig. 9. (a) and (b) Trace element plots showing the adakitic character of felsic rocks from NE Iran, compared with possibly parental mafic, arc-like rocks from the same region, and the OIB-like alkali basalts. Fields and Meshkan Triangle data from Shabanian et al. (2012). (c) and (d) Comparison of chondrite-normalised and primitive mantle-normalised trace element patterns between the felsic adakite-like rocks, mafic arc-like rocks and OIB-like alkali basalts. Meshkan data from Shabanian et al. (2012) and average Phanerozoic adakites (both low- and high-SiO_2 varieties) from Condie (2005).

Lower crustal melting models for adakites can also be ruled out if a petrogenetic link to more mafic, mantle-derived magmas can be proven (Macpherson et al., 2006). Shabanian et al. (2012) reported four analyses of Late Cenozoic mafic lavas in the Meshkan Triangle (Fig. 7a–d). These rocks are unlike the OIB-like lavas of our study as they have Sr/Y and La/Yb ratios which lie at the high and low ends of the arc and adakite fields, respectively (Fig. 9a and b). The mafic Meshkan rocks also have slight HREE depletion along with moderately high LREE/HFSE and LILE/HFSE ratios (Fig. 9c–d) which could be consistent an origin by melting of a subduction-modified source (i.e. the Eastern Iranian lithospheric mantle). That said, the Nb–Ta anomalies depicted for these mafic rocks in Fig. 9d are not prominent, so it is cautioned that these are not 'typical arc rocks' which display large negative Nb–Ta anomalies. An alternative explanation is that these mafic samples had OIB-like parents, but unlike the Quchan, Binalud and Nayband/Neh OIB-like basalts which are the main focus of this paper, these may have experienced very extensive crustal contamination and fractionation during their ascent, resulting in destruction of any OIB-like trace element signature. Detailed trace element and isotopic evidence would be required to understand the contamination history of these mafic rocks.

Nevertheless, if the mafic magmas generated in NE Iran were to fractionate garnet and/or amphibole during their ascent, which are compatible with the M-HREE, they would form adakite-like daughter products with high Sr/Y (Macpherson et al., 2006). Richards et al. (2012) have also proposed that suppressed plagioclase fractionation under hydrous conditions generated high-Sr/Y adakites beneath SW Iran. Given that in Fig. 9c and d the Meshkan mafic rocks have mostly similar overall trace element patterns compared with the adakite-like rocks, it is quite possible that the mafic rocks represent parental magmas to the latter. The key difference between the mafic magmas of Shabanian et al. (2012) and the adakites is that the adakites have significantly larger negative Nb–Ta anomalies. This may be caused by extensive amphibole fractionation and/or crustal contamination from a more OIB-like parent.

Our favoured model for melt generation beneath NE Iran therefore involves melting of the uppermost asthenosphere or lowermost melt-metasomatised lithospheric mantle to generate the OIB-like alkali basalts. There may have been fusion of a distinct subduction-modified lithospheric mantle to generate basaltic magmas. The latter may have evolved towards adakite-like compositions during ascent, or some of the original OIB-like basalts may have been extensively contaminated and fractionated to form the adakites. We do note that the OIB-like basalts from Quchan do not appear to have experienced any interaction with adakite-like melts: they do not have raised SiO_2 or the appearance of negative HFSE anomalies. This is common in subduction settings, where high-Nb (OIB-like) basalts are penecontemporaneous with adakites and in some cases arc basalts, but appear to have little identifiable chemical interaction with one another (e.g., Castillo et al., 2002; Macpherson et al., 2010; Sorbadere et al., 2013; Neill et al., 2013b). The various magmas in such settings may simply be derived from different source regions and take different pathways to the surface.

6. Explanations for OIB-like magmatism during continental collision

6.1. Localised or regional extension

Although mafic magmas can be emplaced in compressive tectonic regimes where they exploit crustal weaknesses caused by reverse faulting (e.g., Tibaldi, 2005), all three magmatic regions here have previously been linked to localised extension and/or lithospheric delamination. The mafic and felsic rocks of the Meshkan area were emplaced in a tectonic wedge which generated accommodation space (Shabanian et al., 2012). This scenario is similar to the confluence of the North and East Anatolian faults in Turkey, where extensive magmatism occurs around the Bingol, Nemrut and Muş volcanoes (Pearce et al., 1990). Further south in Iran, the Nayband and Neh faults are strike-slip systems which can contain transtensional segments (Walker et al., 2009; Pang et al., 2012) which would be ideal locations for magmatic activity. The Neh Fault also follows the Sistan suture which marks the eastern boundary of the Lut Block, whereas the Nayband Fault separates the Lut and Tabas Blocks of the Central Iranian Microcontinent (Fig. 1b), so magmatic activity may also be focussed on pre-existing crustal weaknesses regardless of Late Cenozoic fault motion. Finally, the Binalud alkali basalt cone lies at the termination of the curved trace of the left-lateral Doruneh Fault (Fig. 1b). A similar example of magmatism associated with curved fault traces is found in Armenia, where Pliocene–Quaternary lavas have been erupted either side of the path of the Pambak-Sevan-Syunik fault system (Neill et al., 2013a). Saadat and Stern (2012) argued that the Binalud centre was also related to the Neh Fault, such that the Binalud cone lay at the junction of the Neh and Doruneh Faults in a pull-apart zone. However, the Neh Fault cannot be traced any closer than ~250 km from the eruption site. We prefer that the location of the Binalud centre is controlled by tension associated with the termination of the Doruneh Fault, similar to the trailing imbricate fan model of Woodcock and Fischer (1986). Nevertheless, it seems unlikely that magma generation itself was the result of crustal-scale faulting given the overall compressive tectonic regime. Deeper lithospheric or asthenospheric processes are therefore required to explain partial melting.

6.2. Processes in the deep lithosphere and upper asthenosphere

Iran has experienced a long history of subduction-related activity and the upper mantle will have been modified by subduction-related fluids and/or melts at various times since the Mesozoic (e.g., Su et al., 2014). 'Wetting' of the upper asthenosphere and lower lithosphere can result in lowered mantle viscosity and thus enhanced small-scale patterns of mantle convection (Hernlund et al., 2008; Kaislaniemi et al., 2014). Such small-scale convection is likely to lead to localised convective removal of the lowermost lithosphere in collision settings as well as decompression melting of upwelling asthenosphere to form OIB-like magmas (Elkins-Tanton, 2007; Kaislaniemi et al., 2014). The modelling of Kaislaniemi et al. (2014) simulated the delamination of pockets of lithospheric mantle << 100 km across which would not be picked up during seismic studies. This localised delamination may also result in heating of the lowermost (subduction-modified) lithospheric mantle by advection and exposure to hot asthenosphere (Elkins-Tanton, 2007) which would provide a sensible explanation for the generation of any magmas with primary arc-like features such as negative Nb–Ta anomalies.

Tomography indicates low V_s beneath the Lut Block at ~100 km depth, with this pattern extending across Central Iran, the Alborz, NW Iran, Eastern Anatolia and the Caucasus (Manaman et al., 2011). Positive V_s anomalies are observed at a similar depth beneath the Binalud-Meshkan area (Manaman et al., 2011), which has been argued to be consistent with extensive patches of pyroxenitic lithologies (Su et al., 2014). The overall lithospheric thickness is considered to be ~110–140 km across much of Eastern Iran (Priestley et al., 2012; Motaghi et al., in press), such that these anomalies lie in the lithospheric mantle or the very uppermost parts of the asthenosphere. The low V_s anomaly may represent small fractions of partial melt, although the depth of the anomaly

is somewhat greater than geochemical studies indicate for melting across the region (garnet–spinel transition; Walker et al., 2009; Saadat and Stern, 2012). The anomaly is also unlikely to represent higher than ambient mantle temperatures. Recent isotopic studies have disproven a link between the closest within-plate foreland magmatism to Turkey and Iran at the Karacadag volcanic centre in Northern Arabia, and the Afar plume (Ekici et al., 2014). Secondly, OIB-like output in Iran is extremely limited, with only small-volume cones and flows as opposed to more extensive magmatic outpourings which might be expected with a hotter-than-ambient mantle source.

One possibility is that the low V_s region beneath the Lut Block is the result of addition of small volumes of fluid related to Tethyan subduction processes – either from slabs that have broken off during the Cenozoic and now lie within the transition zone, or from active subduction. Manaman et al. (2011) coupled S-wave tomography and earthquake data to demonstrate that the Makran subduction zone dips very shallowly to reach only ~75 km on its upper surface beneath arc volcanoes in Southern Iran. Inboard from there, the high V_s anomaly associated with the slab dips more steeply and eventually fades out at depths of 200–250 km beneath the central part of the Lut Block. The low seismic velocity region lies directly above this slab and beneath the Lut Block, so it is possible that it corresponds to slightly hydrated mantle in the Makran back arc.

There may also be a role for edge-driven convection in melt generation (e.g., King and Anderson, 1998; Kaislaniemi and van Hunen, 2014), given that there is a significant lithospheric thickness gradient on the eastern side of the >200 km thick Zagros lithosphere (Priestley et al., 2012). This pattern may not be easily recognised in the volcanic record, however, given that magmatic activity could also be focussed preferentially into the Nayband and Neh Fault systems by the presence of strong lithosphere in the Lut Block.

7. Conclusions

OIB-like alkali basalts erupted sporadically from the Oligocene to the Quaternary over Eastern Iran. Emplacement has occurred chiefly in relation to localised extension in what remains an overall compressive tectonic regime during the ongoing Arabia–Eurasia collision, but extension is unlikely to have controlled initial melt generation. The lavas are sourced from a heterogeneous, possibly asthenospheric source containing DMM and EMII components, with involvement of melts derived from the garnet stability field. Felsic, adakite-like rocks were erupted or emplaced over a slightly longer time period than the mafic rocks and may have formed by high pressure fractionation of basaltic magmas. The Eastern Iranian mafic rocks are an example of magmatism of within-plate character within an active continental collision zone without involvement of a mantle plume or subduction components in their petrogenesis. Much more extensive melting of lithospheric mantle and crustal sources has occurred further west within the Turkish–Iranian Plateau, where the plateau lithosphere is «100 km thick, but nevertheless OIB-like input can also be detected in some centres in Eastern Anatolia (Parlak et al., 2001; Kheirkhah et al., 2009; Özdemir et al., 2006; Özdemir and Güleç, 2014). We propose that slightly hydrated, low-viscosity mantle lies beneath the collision zone, caused by the dewatering of oceanic slabs either during subduction or from deeper-lying slab material within the mantle transition zone. Such mantle is capable of vigorous convection, causing small-scale delamination events and decompression melting (Kaislaniemi et al., 2014). Heating and melting of the base of the remaining subduction-modified lithosphere can also occur during small-scale delamination.

Acknowledgements

Research was funded by the Natural Environment Research Council (UK) Standard Grant [NE/H021620/1] 'Orogenic Plateau Magmatism'. The Geological Survey of Iran are thanked for their support over many years. Nick Marsh carried out XRF analyses at the University of Leicester and Geoff Nowell and Chris Ottley helped with elemental and isotopic analysis at the Durham Geochemistry Centre. We thank John Adam and two anonymous reviewers for their comments which have collectively improved this manuscript.

References

Aldanmaz, E., Koprubasi, N., Gurer, O.F., Kaymakci, N., Gourgaud, A., 2006. Geochemical constraints on the Cenozoic, OIB-type alkaline volcanic rocks of NW Turkey: implications for mantle sources and melting processes. Lithos 86, 50–76.

Allen, M.B., Armstrong, H.A., 2008. Arabia–Eurasia collision and the forcing of mid Cenozoic global cooling. Palaeontol. Palaeoclimatol. Palaeoecol. 265, 52–58.

Allen, M.B., Kheirkhah, M., Neill, I., Emami, M.H., McLeod, C.L., 2013a. Generation of arc and within-plate chemical signatures in collision zone magmatism: quaternary lavas from Kurdistan Province, Iran. J. Petrol. 54, 887–911.

Allen, M.B., Saville, C., Blanc, E.J.-P., Talebian, M., Nissen, E., 2013b. Orogenic plateau growth: expansion of the Turkish-Iranian Plateau across the Zagros fold-and-thrust belt. Tectonics 32, 171–190.

Angus, D.A., Wilson, D.C., Sandvol, E., Ni, J.F., 2006. Lithospheric structure of the Arabian and Eurasian collision zone in eastern Turkey from S-wave receiver functions. Geophys. J. Int. 166, 1335–1346.

Atherton, M.P., Ghani, A.A., 2002. Slab breakoff: a model for Caledonian, Late Granite syn-collisional magmatism in the orthotectonic (metamorphic) zone of Scotland and Donegal, Ireland. Lithos 62, 65–85.

Atherton, M.P., Petford, N., 1993. Generation of sodium-rich magmas from newly underplated basaltic crust. Nature 362, 144–146.

Barry, T.L., Kent, R.W., 1998. Cenozoic magmatism in Mongolia and the origin of Central and East Asian basalts. In: Flower, M.F.J., Chung, S.-L., Lo, C.-H., Lee, T.-Y. (Eds.), Mantle Dynamics and Plate Interactions in East Asia. AGU Geodynamics Book Series 27, American Geophysical Union, Washington, D.C., pp. 347–364.

Bauman, A., Spies, O., Lensch, G., 1983. Strontium isotopic composition of post-ophiolitic Tertiary volcanics between Kashmar, Sabzevar and Quchan/NE Iran. Geodynamic Project (Geotraverse) in Iran, Report Number 51, Geological Survey of Iran, Tehran, pp. 267–276.

Beccaluva, L., Bianchini, G., Natali, C., Siena, F., 2011. Geodynamic control on orogenic and anorogenic magmatic phases in Sardinia and Southern Spain: inferences for the Cenozoic evolution of the western Mediterranean. Lithos 123, 218–224.

Bottrill, A.D., van Hunen, J., Allen, M.B., 2012. Insight into collision zone dynamics from topography: numerical modelling results and observations. Solid Earth 3, 387–399.

Castillo, P.R., Solidum, R.U., Runongbayan, R.S., 2002. Origin of high field strength element enrichment in the Sulu Arc, southern Philippines, revisited. Geology 30, 707–710.

Chauvel, C., Lewin, E., Carpentier, M., Arndt, N.T., Marini, J.-C., 2008. Role of recycled oceanic basalt and sediment in generating the Hf–Nd mantle array. Nat. Geosci. 1, 64–67.

Chiu, H.-Y., Chung, S.-L., Zarrinkoub, M.H., Mohammadi, S.S., Khatib, M.M., Ijzuka, Y., 2013. Zircon U/Pb constraints from Iran on the magmatic evolution related to Neotethyan subduction and Zagros orogeny. Lithos 162, 70–87.

Condie, K.C., 2005. TTGs and adakites: are they both slab melts? Lithos 80, 33–44.

Davies, J.H., von Blanckenburg, F., 1995. Slab breakoff: a model of lithosphere detachment and its test in the magmatism and deformation of collisional orogens. Earth Planet. Sci. Lett. 129, 85–102.

Defant, M.J., Drummond, M.S., 1990. Derivation of some modern arc magmas by partial melting of young subducted lithosphere. Nature 347, 662–665.

Dilek, Y., Imamverdiyev, N., Altunkaynak, Ş., 2010. Geochemistry and tectonics of Cenozoic volcanism in the Lesser Caucasus (Azerbaijan) and the peri-Arabian region: collision-induced mantle dynamics and its magmatic signature. Int. Geol. Rev. 52, 536–578.

Dowall, D.P., Nowell, G.M., Pearson, D.G., 2007. Chemical pre-concentration procedures for high-precision analysis of Hf–Nd–Sr isotopes in geological materials by plasma ionisation multi-collector mass spectrometry (PIMSS) techniques. In: Holland, J.G., Tanner, S.D. (Eds.), Plasma Source Mass Spectrometry: Applications and Emerging Technologies. The Royal Society of Chemistry, Cambridge, pp. 321–337.

Dupré, B., Allègre, C.J., 1983. Pb–Sr isotope variation in Indian Ocean basalts and mixing phenomena. Nature 303, 142–146.

Ekici, T., Macpherson, C.G., Otlu, N., Fontignie, D., 2014. Foreland magmatism during the Arabia–Eurasia collision: Pliocene–Quaternary activity of the Karacadağ Volcanic Complex, SW Turkey. J. Petrol. 55, 1753–1777.

Elkins-Tanton, L.T., 2007. Continental magmatism, volatile recycling, and heterogeneous mantle caused by lithospheric gravitational instabilities. J. Geophys. Res. 112, B03405. http://dx.doi.org/10.1029/2005JB004072.
Emami, M.H., Sadeghi, M.M.M., Omrani, S.J., 1993. Magmatic map of Iran. Tehran, Geol. Surv. Iran, 1 sheet.
Galer, S.J.G., 1997. Optimal triple spiking for high precision lead isotope ratio determination. Terra Nova Supp. 9, 441.
Geological Survey of Iran, 1984. Geological Map of Faruj. Map 076, 1:100,000 scale, 1 sheet.
Ghasemi, H., Sadeghian, M., Khan Alizadeh, A.R., Tanha, A., 2010. Petrology, geochemistry and radiometric ages of silica adakitic domes of Neogene continental arc, south of Quchan [in Persian with English abstract]. Iran. J. Crystallogr. Mineral. 18, 347–370.
Gibson, S.A., Thompson, R.N., Day, J.A., Humphris, S.E., Dickin, A.P., 2005. Melt-generation processes associated with the Tristan mantle plume: constraints on the origin of EM-1. Earth Planet. Sci. Lett. 237, 744–767.
Hart, S.R., 1984. A large-scale isotope anomaly in the Southern Hemisphere mantle. Nature 309, 753–757.
Hastie, A.R., Kerr, A.C., McDonald, I., Mitchell, S.F., Pearce, J.A., Millar, I.L., Barfod, D., Mark, D.F., 2010. Geochronology, geochemistry and petrogenesis of rhyodacite lavas in eastern Jamaica: a new adakite subgroup analogous to early Archaean continental crust? Chem. Geol. 276, 344–359.
Hastie, A.R., Mitchell, S.F., Kerr, A.C., Minifie, M.J., Millar, I.L., 2011. Geochemistry of rare high-Nb basalt lavas: are they derived from a mantle wedge metasomatised by slab melts? Geochim. Cosmochim. Acta 75, 5049–5072.
Hastie, A.R., Mitchell, S.F., Treloar, P.J., Kerr, A.C., Neill, I., Barfod, D.N., 2013. Geochemical components in a Cretaceous island arc: the Th/La–$(Ce/Ce^{*})_{Nd}$ diagram and implications for subduction initiation in the inter-American region. Lithos 162–163, 57–69.
Haxby, W.F., Melkonian, A.K., Coplan, J., Chan, S.-M., Ryan, W.B.F., 2010. GeoMapApp freeware software, v. 3.3.9. Lamon-Doherty Earth Observatory, Palisades, NY.
Hernlund, J.W., Tackley, P.J., Stevenson, D.J., 2008. Buoyant melting instabilities beneath extending lithosphere: 1. Numerical models. J. Geophys. Res. 113, B04405. http://dx.doi.org/10.1029/2006JB004862.
Holt, P.J., Allen, M.B., van Hunen, J., Bjørnseth, H.M., 2010. Lithospheric cooling and thickening as a basin forming mechanism. Tectonophysics 495, 184–194.
Ingle, S., Weis, D., Doucet, S., Mattielli, N., 2003. Hf isotope constraints on mantle sources and shallow-level contaminants during Kerguelen hot spot activity since ~120 Ma. Geochem. Geophys. Geosyst. 4, 1068. http://dx.doi.org/10.1029/2002GC000482.
Ionov, D.A., Dupuy, C., O'Reilly, S.Y., Kopylova, M.G., Genshaft, Y.S., 1993. Carbonated peridotite xenoliths from Spitsbergen: implications for trace element signature of mantle carbonate metasomatism. Earth Planet. Sci. Lett. 119, 283–297.
Kaislaniemi, L., van Hunen, J., 2014. Dynamics of lithospheric thinning and mantle melting by edge-driven convection: application to Moroccan Atlas mountains. Geochem. Geophys. Geosyst. 15, 3175–3189.
Kaislaniemi, L., van Hunen, J., Allen, M.B., Neill, I., 2014. Sublithospheric small-scale convection: a mechanism for collision magmatism. Geology 42, 291–294.
Keskin, M., 2003. Magma generation by slab steepening and breakoff beneath a subduction-accretion complex: an alternative model for collision-related volcanism in Eastern Anatolia, Turkey. Geophys. Res. Lett. 30, 1–4.
Kheirkhah, M., Allen, M.B., Emami, M.H., 2009. Quaternary syn-collision magmatism from the Iran/Turkey borderlands. J. Volcanol. Geoth. Res. 182, 1–12.
Kheirkhah, M., Neill, I., Allen, M.B., Ajdari, K., 2013. Small-volume melts of lithospheric mantle during continental collision: late Cenozoic lavas of Mahabad, NW Iran. J. Asian Earth Sci. 74, 37–49.
King, S.D., Anderson, D.L., 1998. Edge-driven convection. Earth Planet. Sci. Lett. 160, 289–296.
Le Maitre, R.W., Streckeisen, A., Zanettin, B., Le Bas, M.J., Bonin, B., Bateman, P., Bellieni, G., Dudek, A., Efremova, S., Keller, J., Maere, J., Sabine, P.A., Schmid, R., Sorensen, H., Woolley, R., 2002. Igneous rocks: a classification and glossary of terms. Recommendations of the International Union of Geological Sciences, Subcommission on the Systematics of Igneous Rocks. Cambridge University Press.
Lebedev, S., Meier, T., van der Hilst, R.D., 2006. Asthenospheric flow and origin of volcanism in the Baikal Rift area. Earth Planet. Sci. Lett. 249, 415–424.
Liu, X.-J., Xu, J.-F., Castillo, P.R., Xiao, W.-J., Shi, Y., Feng, Z.-H., Guo, L., 2014. The Dupal isotopic anomaly in the southern Paleo-Asian Ocean: Nd–Pb isotope evidence from ophiolites in Northwest China. Lithos 189, 185–200.
Lustrino, M., Wilson, M., 2007. The circum-Mediterranean anorogenic Cenozoic igneous province. Earth Sci. Rev. 81, 1–65.
Macpherson, C.G., Dreher, S.T., Thirlwall, M.F., 2006. Adakites without slab melting: high pressure processing of basaltic island arc magma, Mindanao, the Philippines. Earth Planet. Sci. Lett. 243, 581–593.
Macpherson, C.G., Chiang, K.K., Hall, R., Nowell, G.M., Castillo, P.R., Thirlwall, M.F., 2010. Plio-Pleistocene intra-plate magmatism from the southern Sulu Arc, Semporna peninsula, Sabah, Borneo: implications for high-Nb basalt in subduction zones. J. Volcanol. Geoth. Res. 190, 25–38.
Manaman, N.S., Shomali, H., Koyi, H., 2011. New constraints on upper-mantle S-velocity structure and crustal thickness of the Iranian plateau using partitioned waveform inversion. Geophys. J. Int. 184, 247–267.
McDonough, W.F., Sun, S.-S., 1995. The composition of the Earth. Chem. Geol. 120, 223–253.
McQuarrie, N., van Hinsbergen, D.J.J., 2013. Retrodeforming the Arabia-Eurasia collision zone: age of collision versus magnitude of continental subduction. Geology 41, 315–318.
Meyzen, C.M., Ludden, J.N., Humler, E., Luais, B., Toplis, M.J., Mével, C., Storey, M., 2005. New insights into the origin and distribution of the DUPAL isotope anomaly in the Indian Ocean mantle from MORB of the Southwest Indian Ridge. Geochem. Geophys. Geosyst. 6, Q11K11. http://dx.doi.org/10.1029/2005GC000979.
Motaghi, K., Tatar, M., Shomali, Z.H., Kaviani, A., Priestley, K., 2012. High resolution image of the uppermost mantle beneath NE Iran continental collision zone. Phys. Earth Planet. Inter. 208–209, 38–49.
Motaghi, K., Tatar, M., Priestley, K., Romanelli, F., Doglioni, C., Panza, G.F. The deep structure of the Iranian Plateau. Gondwana Research (in press), doi:http://dx.doi.org/10.1016/j.gr.2014.04.009.
Moyen, J.-F., 2009. High Sr/Y and La/Yb ratios: the meaning of the "adakitic signature". Lithos 112, 556–574.
Neill, I., Meliksetian, Kh., Allen, M.B., Navasardyan, G., Kuiper, K., in press. Petrogenesis of mafic collision zone magmatism: The Armenian sector of the Turkish-Iranian Plateau, Chemical Geology. http://dx.doi.org/10.1016/j.chemgeo.2015.03.013.
Neill, I., Meliksetian, Kh., Allen, M.B., Navasardyan, G., Karapetyan, S., 2013a. Pliocene–Quaternary volcanic rocks of NW Armenia: magmatism and lithospheric dynamics within an active orogenic plateau. Lithos 180–181, 200–215.
Neill, I., Kerr, A.C., Hastie, A.R., Pindell, J.L., Millar, I.L., 2013b. The Albian–Turonian island arc rocks of Tobago, West Indies: geochemistry, petrogenesis, and Caribbean Plate tectonics. J. Petrol. 54, 1607–1639.
Nowell, G.M., Kempton, P.D., Noble, S.R., Fitton, J.G., Saunders, A.D., Mahoney, J.J., Taylor, R.N., 1998. High precision Hf isotope measurements of MORB and OIB by thermal ionisation mass spectrometry: insights into the depleted mantle. Chem. Geol. 149, 211–233.
Özdemir, Y., Güleç, N., 2014. Geological and geochemical evolution of the Quaternary Süphan stratovolcano, Eastern Anatolia, Turkey: evidence for the lithosphere–asthenosphere interaction in post-collision volcanism. J. Petrol. 55, 37–52.
Özdemir, Y., Karaoğlu, Ö., Tolluoğlu, A.Ü., Güleç, N., 2006. Volcanostratigraphy and petrogenesis of the Nemrut stratovolcano (East Anatolian High Plateau): the most recent post-collisional volcanism in Turkey. Chem. Geol. 226, 189–211.
Pang, K.-N., Chung, S.-L., Zarrinkoub, M.H., Mohammadi, S.S., Yang, H.-M., Chu, C.-H., Lee, H.-Y., Lo, C.-H., 2012. Age, geochemical characteristics and petrogenesis of Late Cenozoic intraplate alkali basalts in the Lut–Sistan region, eastern Iran. Chem. Geol. 306–307, 40–53.
Pang, K.-N., Chung, S.-L., Zarrinkoub, M.H., Lin, Y.-C., Lee, H.-Y., Lo, C.-H., Khatib, M.M., 2013. Iranian ultrapotassic volcanism at ~11 Ma signifies the initiation of post-collision magmatism in the Arabia–Eurasia collision zone. Terra Nova 25, 405–413.
Pang, K.-N., Chung, S.-L., Zarrinkoub, M.H., Chiu, H.-Y., Li, X.-H., 2014. On the magmatic record of the Makran Arc, southeastern Iran: insights from zircon U–Pb geochronology and bulk-rock geochemistry. Geochem. Geophys. Geosyst. 15. http://dx.doi.org/10.1002/2014GC005262.
Parlak, O., Delaloye, M., Demirkol, C., Ünlügenç, U.C., 2001. Geochemistry of Pliocene/Pleistocene basalts along the Central Anatolian Fault Zone (CAFZ), Turkey. Geodin. Acta 14, 159–167.
Paul, A., Hatzfeld, D., Kaviani, A., Tatar, M., Péquegnat, C., 2010. Seismic imaging of the lithospheric structure of the Zagros mountain belt (Iran). In: Leturmy, P., Robin, C. (Eds.), Tectonic and Stratigraphic Evolution of Zagros and Makran during the Mesozoic-Cenozoic. Geological Society of London Special Publication 330, pp. 5–18.
Pearce, J.A., Peate, D.W., 1995. Tectonic implications of the composition of volcanic arc magmas. Ann. Rev. Earth Planet. Sci. Lett. 23, 251–285.
Pearce, J.A., Bender, J.F., Delong, S.E., Kidd, W.S.F., Low, P.J., Guner, Y., Sargolu, F., Yilmaz, Y., Moorbath, S., Mitchell, J.G., 1990. Genesis of collision volcanism in eastern Anatolia, Turkey. J. Volcanol. Geoth. Res. 44, 189–229.
Peccerillo, R., Taylor, S.R., 1976. Geochemistry of Eocene calc-alkaline volcanic rocks from the Kastamonu area, northern Turkey. Contrib. Miner. Petrol. 58, 63–81.
Plank, T., 2005. Constraints from Thorium/Lanthanum on Sediment Recycling at Subduction Zones and the Evolution of the Continents. J. Petrol. 46, 921–944.
Priestley, K., McKenzie, D., Barron, J., Tatar, M., Debayle, E., 2012. The Zagros core: deformation of the continental lithospheric mantle. Geochem. Geophys. Geosyst. 13. http://dx.doi.org/10.1029/2012GC004435.
Rapp, R.P., Watson, E.B., 1995. Dehydration melting of metabasalt at 8–32 kbar: implications for continental growth and crust-mantle recycling. J. Petrol. 36, 891–931.
Richards, J.P., Spell, T., Rameh, E., Razique, A., Fletcher, T., 2012. High Sr/Y magmas reflect arc maturity, high magmatic water content, and porphyry Cu ± Mo ± Au potential: examples from the Tethyan arcs of Central and Eastern Iran and Western Pakistan. Econ. Geol. 107, 295–332.
Rudnick, R.L., McDonough, W.F., Chappell, B.W., 1993. Carbonatite metasomatism in the northern Tanzanian mantle: petrographic and geochemical characteristics. Earth Planet. Sci. Lett. 114, 463–475.
Ryan, W.B.F., Carbotte, S.M., Coplan, J.O., O'Hara, S., Melkonian, A., Arko, R., Weissel, R.A., Ferrini, V., Goodwillie, A., Nitsche, F., Bonczkowski, J., Zemsky, R., 2009. Global multi-resolution topography synthesis. Geochem. Geophys. Geosyst. 10, Q03014. http://dx.doi.org/10.1029/2008GC00232.
Saadat, S., Stern, C.R., 2011. Petrochemistry and genesis of olivine basalts from small monogenetic parasitic cones of Bazman stratovolcano, southeastern Iran. Lithos 125, 609–617.
Saadat, S., Stern, C.R., 2012. Petrochemistry of a xenolith-bearing Neogene alkali olivine basalt from northeastern Iran. J. Volcanol. Geoth. Res. 225, 13–29.

Saadat, S., Stern, C.R., 2014. Petrochemistry of ultrapotassic tephrites and associated cognate plutonic xenoliths from late Quaternary Qa'le Hasan Ali maars, Central Iran. J. Asian Earth Sci. 89, 108–122.
Saadat, S., Karimpour, M.H., Stern, C.R., 2010. Petrochemical characteristics of Neogene and Quaternary alkali olivine basalts from the western margin of the Lut Block, Eastern Iran. Iran. J. Earth Sci. 2, 87–106.
Saal, A.E., Hart, S.R., Shimizu, N., Hauri, E.H., Layne, G.D., Eiler, J.M., 2005. Pb isotopic variability in melt inclusions from the EMI–EMII–HIMU mantle end-members and the role of the oceanic lithosphere. Earth Planet. Sci. Lett. 240, 605–620.
Seltmann, R., Konopelko, D., Biske, G., Divaev, F., Sergeev, S., 2011. Hercynian post-collisional magmatism in the context of Paleozoic magmatic evolution of the Tien Shan orogenic belt. J. Asian Earth Sci. 42, 821–838.
Şengör, A.M.C., 1984. The Cimmeride Orogenic System and the tectonics of Eurasia. Geological Society of America Special Paper 195, 74pp.
Shabanian, E., Acocella, V., Gioncada, A., Ghasemi, H., Bellier, O., 2012. Structural control on volcanism in intraplate post collisional settings: late Cenozoic to Quaternary examples of Iran and Eastern Turkey. Tectonics 31. http://dx.doi.org/10.1029/2011TC003042.
Shahabpour, J., 2005. Tectonic evolution of the orogenic belt in the region located between Kerman and Neyriz. J. Asian Earth Sci. 24, 405–417.
Shojaat, B., Hassanipak, A.A., Mobasher, K., Ghazi, A.M., 2003. Petrology, geochemistry and tectonics of the Sabzevar ophiolite, North Central Iran. J. Asian Earth Sci. 21, 1053–1067.
Sobolev, A.V., Hofmann, A.W., Sobolev, S.V., Nikogosian, I.K., 2005. An olivine-free mantle source of Hawaiian shield basalts. Nature 434, 590–597.
Sorbadere, F., Schiano, P., Métrich, N., Bertagnini, A., 2013. Small-scale co-existence of island-arc- and enriched-MORB-type basalts in the central Vanuatu arc. Contrib. Miner. Petrol. 166, 1305–1321.
Spies, O., Lensch, G., Mihem, A., 1983. Geochemistry of the postophiolitic Tertiary volcanics between Sabzevar and Quchan (NE Iran). Rep. Geol. Mineral. Surv. Iran 51, 247–266.
Su, B.-X., Chung, S.-L., Zarrinkoub, M.H., Pang, K.-N., Chen, L., Ji, W.-Q., Brewer, A., Ying, J.-F., Khatib, M.M., 2014. Composition and structure of the lithospheric mantle beneath NE Iran: constraints from mantle xenoliths. Lithos 202–203, 267–282.
Sun, S.-S., McDonough, W.F., 1989. Chemical and isotopic systematics of oceanic basalts: implications for mantle composition and processes. In: Saunders, A.D., Norry, M.J. (Eds.), Magmatism in the Ocean Basins: Geological Society of London Special Publicatin, vol. 42, pp. 313–345.
Taylor, S.R., McLennan, S.M., 1985. The continental crust: Its composition and evolution. Oxford, 311pp.
Tibaldi, A., 2005. Volcanism in compressional tectonic settings: is it possible? Geophys. Res. Lett. 32, L06309. http://dx.doi.org/10.1029/2004GL021798.
Turner, S., Sandiford, M., Foden, J., 1992. Some geodynamic and compositional constraints on 'postorogenic' magmatism. Geology 20, 931–934.
Vernant, P., Nilfouroushan, F., Hatzfeld, D., Abbassi, M.R., Vigny, C., Masson, F., Nankali, H., Martinod, J., Ashtiani, A., Bayer, R., Tavakoli, F., Chéry, J., 2004. Present-day crustal deformation and plate kinematics in the Middle East constrained by GPS measurements in Iran and northern Oman. Geophys. J. Int. 157, 381–398.
Walker, R.T., Jackson, J., 2004. Active tectonics and late Cenozoic strain distribution in central and eastern Iran. Tectonics 23, TC5010. http://dx.doi.org/10.1029/2003TC001529.
Walker, R.T., Gans, P., Allen, M.B., Jackson, J., Khatib, M., Marsh, N., Zarrinkoub, M., 2009. Late Cenozoic volcanism and rates of active faulting in eastern Iran. Geophys. J. Int. 177, 783–805.
Wang, K.-L., Chung, S.-L., O'Reilly, S.Y., Sun, S.-S., Shinjo, R., Chen, C.-H., 2004. Geochemical constraints for the genesis of post-collisional magmatism and the geodynamic evolution of the Northern Taiwan region. J. Petrol. 45, 975–1011.
Williams, H.M., Turner, S.P., Pearce, J.A., Kelley, S.P., Harris, N.B.W., 2004. Nature of the source regions for post-collisional potassic magmatism in southern and northern Tibet from geochemical variations and inverse trace element modelling. J. Petrol. 45, 555–607.
Wilson, M., Downes, H., 2006. Tertiary-Quaternary intra-plate magmatism in Europe and its relationship to mantle dynamics. In: Gee, D.G., Stephenson, R. (Eds.), European lithosphere dynamics. Geological Society of London Memoir 32, pp. 147–166.
Woodcock, N.H., Fischer, M., 1986. Strike-slip duplexes. J. Struct. Geol. 8, 725–735.
Zhang, J., Zhao, Z.-F., Zheng, Y.-F., Dai, M., 2010. Postcollisional magmatism: geochemical constraints on the petrogenesis of Mesozoic granitoids in the Sulu orogen, China. Lithos 119, 512–536.
Zhao, D., Tian, Y., Lei, J., Liu, L., Zheng, S., 2009. Seismic image and origin of the Changbai intraplate volcano in East Asia: role of big mantle wedge above the stagnant Pacific slab. Phys. Earth Planet. Inter. 173, 197–206.
Zhao, Z.-F., Dai, L.-Q., Zheng, J.-F., 2013. Postcollisional mafic igneous rocks record crust-mantle interaction during continental deep subduction. Nat. Sci. Rep. 3. http://dx.doi.org/10.1038/srep03413.
Zor, E., 2008. Tomographic evidence of slab detachment beneath eastern Turkey and the Caucasus. Geophys. J. Int. 175, 1273–1282.